Conceptual and probabilistic comparison of DIA-estimators for bias-known hypothesis testing

Zaminpardaz, S.; Teunissen, P. J.G.

DOI
10.1007/s00190-025-01977-z

Publication date
2025

Document Version
Final published version

Published in
Journal of Geodesy

Citation (APA)
Zaminpardaz, S., & Teunissen, P. J. G. (2025). Conceptual and probabilistic comparison of DIA-estimators for bias-known hypothesis testing. *Journal of Geodesy*, *99*(8), Article 64. https://doi.org/10.1007/s00190-025-01977-z

Journal of Geodesy (2025) 99:64
https://doi.org/10.1007/s00190-025-01977-z

ORIGINAL ARTICLE

Conceptual and probabilistic comparison of DIA-estimators for bias-known hypothesis testing

S. Zaminpardaz[1] · P. J. G. Teunissen[2,3,4]

Received: 3 February 2025 / Accepted: 27 May 2025

Abstract
This contribution investigates four members of the class of Detection, Identification, and Adaptation (DIA) estimators, which integrate parameter estimation with hypothesis testing. Using the framework of minimum mean penalty testing, we analyze and compare the misclosure-space partitionings of the traditional DIA procedure, which combines the overall model test with likelihood-ratio-based tests, and those maximizing the probabilities of correct hypothesis identification and parameter estimation. A constrained version of the latter, with the null hypothesis acceptance region fixed to the traditional procedure, is also examined. Our study focuses on cases where the biases under alternative hypotheses are fully known. Next to the conceptual comparison, we also assess, through a number of examples, misclosure-space partitionings and the probabilities of DIA estimators falling within a defined elliptical safety region. The results highlight the relationships and distinctions among the DIA estimators, revealing the influence of penalty functions, bias magnitude, safety region size, and false alarm probability.

Keywords Detection-identification-adaptation (DIA) · DIA-estimator · Misclosure space partitioning · Minimum mean penalty testing · Penalty function

1 Introduction

The DIA method for detection, identification, and adaptation of modeling errors integrates parameter estimation with hypothesis testing. This integration is formally encapsulated in the DIA-estimator introduced by Teunissen (2018). Combining estimation with testing has been widely applied across various domains, including the quality control of geodetic networks (DGCC 1982; Amiri Simkooei 2001; Zaminpardaz and Teunissen 2019; Yang et al. 2021; Zaminpardaz and Teunissen 2022; Rofatto et al. 2022), navigational integrity (Teunissen 1990; Gillissen and Elema 1996; Yang et al. 2014), deformation analysis and structural health monitoring (Verhoef and De Heus 1995; Lehmann and Lösler 2017; Yavaşoğlu et al. 2018; Nowel 2020; Zaminpardaz et al. 2020), and GNSS integrity monitoring (Jonkman and De Jong 2000; Kuusniemi et al. 2004; Hewitson and Wang 2006; Khodabandeh and Teunissen 2016; Zaminpardaz and Teunissen 2020).

The DIA estimator represents a class of estimators, each uniquely characterized by its partitioning of the misclosure space (Teunissen 2024a). Modifying the testing procedure results in changes to the partitioning, thereby altering the corresponding DIA estimator. Leveraging the concept of penalized testing introduced in (ibid), penalty functions can be assigned to each decision region within the misclosure space, enabling the calculation of the mean penalty for any given partitioning. This framework facilitates the identification of the optimal partitioning by minimizing the mean penalty. Since the minimum mean penalty partitioning is influenced by the choice of penalty functions, different selections can be tailored to specific applications. For instance, one choice may yield a partitioning that maximizes the probability of correct testing decisions, making it advantageous from a testing perspective. Conversely, another choice may opti-

✉ S. Zaminpardaz
safoora.zaminpardaz@rmit.edu.au

P. J. G. Teunissen
p.j.g.teunissen@tudelft.nl

[1] School of Science, RMIT University, Melbourne, Australia

[2] Department of Geoscience and Remote Sensing, Delft University of Technology, Delft, The Netherlands

[3] School of Earth and Planetary Sciences, Curtin University, Perth, Australia

[4] Department of Infrastructure Engineering, The University of Melbourne, Melbourne, Australia

Published online: 23 July 2025

mize the probability of correct parameter estimation, aligning better with estimation objectives.

In this contribution, we study and compare four members from the class of DIA-estimators, whose misclosure-space partitionings are defined based on the concept of minimum mean penalty testing. Our analysis focuses on cases where the biases under the alternative hypotheses are fully known. The partitionings considered correspond to: I) the traditional DIA procedure, which combines the overall model test (OMT) with likelihood-ratio-based tests, and is commonly used in geodetic applications; II) maximizing probability of correct hypothesis identification; and III) maximizing probability of correct parameter estimation. In geodetic applications, the acceptance region of the null hypothesis, $\mathcal{P}_0$, is typically determined through the OMT based on a user-defined false alarm probability. Therefore, we also examine the $\mathcal{P}_0$-constrained version of II and III, where $\mathcal{P}_0$ is defined by the OMT. It will be demonstrated that, when all alternative hypotheses are equally likely, this $\mathcal{P}_0$-constrained variant of II is identical to I.

This contribution is structured as follows. Section 2 provides a brief overview of the DIA method, outlining its inputs and its integration of estimation and testing. It specifies the null and alternative hypotheses and discusses the implementation of the method's testing scheme using a partitioning of the misclosure space. The DIA-estimator and its statistical distribution are then presented for both bias-unknown and bias-known cases. In Sect. 3, we review the concept of penalized testing, detailing the misclosure-space partitionings I, II and III. The relationships between the test statistics of these testing procedures are highlighted, and the conditions under which two hypotheses can be distinguished for each partitioning are discussed.

The DIA-estimators are analyzed and compared in Sect. 4 using three different examples: three repeat measurements of a single quantity, distance measurements in a three-dimensional geodetic network, and height-difference measurements in a leveling network. In all cases, it is assumed that the alternative hypotheses are equally likely. The analysis includes the misclosure-space partitionings and the probabilities of the DIA-estimators falling within an x-centered elliptical safety region. Additionally, the conditions under which the probabilistic properties of these DIA-estimators converge are highlighted. Finally, Sect. 5 provides a summary and conclusions.

We use the following notation: The n-dimensional space of real numbers is denoted by $\mathbb{R}^n$. Random vectors are represented by underlined symbols, e.g., $\underline{x} \in \mathbb{R}^n$ is a random vector, while x is not. The PDF of random vector $\underline{x} \in \mathbb{R}^n$ is denoted by $f_{\underline{x}}(\theta)$, with $\theta \in \mathbb{R}^n$ being its argument. The squared weighted norm of a vector with respect to a positive-definite matrix Q is defined as $\|\cdot\|^2_Q = (\cdot)^T Q^{-1}(\cdot)$. We reserve $\mathcal{H}$ for statistical hypotheses, $\mathcal{P}$ for partitions of the misclosure space, and $\mathcal{N}(x, Q)$ for the normal distribution with mean x and variance matrix Q. The notation $\mathsf{P}(\cdot|\mathcal{H})$, $\mathsf{E}(\cdot|\mathcal{H})$, and $\mathsf{D}(\cdot|\mathcal{H})$ are the probability, expectation and dispersion operators under $\mathcal{H}$, respectively. The m-dimensional vector of ones, vector of zeros and identity matrix are denoted by e_m, 0_m and I_m, respectively. The symbol $\overset{\mathcal{H}}{\sim}$ should be interpreted as 'distributed as ... under $\mathcal{H}$'. The superscripts ^{T} and $^{-1}$ are used to denote the transpose and the inverse of a matrix, respectively.

2 DIA method: an overview

In this section, we provide a brief overview of the DIA method, including its inputs and how it combines the principles of statistical inference, namely estimation and testing.

2.1 Working model and hypothesized misspecifications

The inputs to the DIA procedure consist of the observations to be modeled and a set of candidate observational models, denoted by $\mathcal{H}_0, \mathcal{H}_1, \ldots, \mathcal{H}_k$, where $\mathcal{H}_0$ represents the working (null) hypothesis and $\mathcal{H}_i$ (for $i = 1, \ldots, k$) are the alternative hypotheses capturing different misspecifications in $\mathcal{H}_0$. Assuming these hypotheses cover all the events that can possibly occur, they can be viewed as the outcomes of a discrete random variable $\underline{\mathcal{H}} = \{\mathcal{H}_0, \ldots, \mathcal{H}_k\}$, with each hypothesis $\mathcal{H}_i$ occurring with probability $\mathsf{P}[\mathcal{H}_i]$ for $i = 0, \ldots, k$, such that $\sum_{i=0}^{k} \mathsf{P}[\mathcal{H}_i] = 1$. While it is standard in geodetic literature to assign randomness only to observation errors, in this work we also consider probabilities associated with the hypotheses themselves. This allows for a structured way to reflect prior knowledge or assumptions about the likelihood of different scenarios, and supports a more informed decision-making process within the hypothesis testing framework.

We assume that the null hypothesis, believed to be valid under normal working conditions, is expressed as follows

$$\mathcal{H}_0 : \underline{y} \sim \mathcal{N}\left(A\,x, Q_{yy}\right) \tag{1}$$

where the mean of the random vector of observables $\underline{y} \in \mathbb{R}^m$ is parameterized in the unknown parameter vector $x \in \mathbb{R}^n$ through the known full-rank design matrix $A \in \mathbb{R}^{m\times n}$ ($\mathrm{rank}(A) = n$), and the dispersion of $\underline{y}$ is characterized by the positive-definite variance matrix $Q_{yy} \in \mathbb{R}^{m\times m}$.

The null hypothesis may be misspecified in various ways, including the assumed expectation (mean) of $\underline{y}$, its dispersion, and even its statistical distribution. Here, we focus on alternatives that describe deviations in the mean of $\underline{y}$ from Ax, as these are among the most common errors encountered

in model formulation (Teunissen 2017). Thus, the alternative hypotheses will differ from $\mathcal{H}_0$ only in the mean of $\underline{y}$, taking the form

$$\mathcal{H}_i : \underline{y} \sim \mathcal{N}\left(Ax + C_i b_i, Q_{yy}\right), \ i = 1, \ldots, k \tag{2}$$

where $C_i b_i \in \mathbb{R}^m \setminus \{0\}$ represents the potential bias in the mean of $\underline{y}$, with $[A \ \ C_i] \in \mathbb{R}^{m\times(n+q_i)}$ a known matrix of full rank. In most cases, the vector $b_i \in \mathbb{R}^{q_i}$ is unknown, such as in scenarios involving pseudorange outliers, carrier-phase cycle slips, or ionospheric gradients. However, there are applications where b_i is completely known; this contribution focuses on such cases, which we refer to as *bias-known* examples. For example, in the context of terrestrial surveying, one may confuse two nearby benchmarks when running a level run, where the known bias would be the difference between the known heights of the two benchmarks. It is important to note that, although the biases under the alternative hypotheses are assumed to be known in this study, their actual presence is uncertain and must be assessed through statistical hypothesis testing.

2.2 Hypothesis testing

The detection and identification steps of the DIA method require implementing a testing procedure to select one of the hypothesized models in (1) and (2) based on a specific criterion. This necessitates the presence of redundancy under $\mathcal{H}_0$, i.e. $r = m - n \neq 0$. With redundancy, one can form a misclosure vector as (Teunissen 2024b)

$$\underline{t} = B^T \underline{y} \overset{\mathcal{H}_i}{\sim} \mathcal{N}\left(C_{t_i} b_i, Q_{tt}\right), \ i = 0, \ldots, k \tag{3}$$

with $B \in \mathbb{R}^{m\times r}$ a matrix of $\text{rank}(B) = r$ such that $A^T B = 0$, $C_{t_i} = B^T C_i$ where $C_0 b_0 = 0$, and $Q_{tt} = B^T Q_{yy} B$ the variance matrix of $\underline{t}$. We note that $\underline{t}$ has a *known* probability distribution under $\mathcal{H}_0$, which is a zero-mean normal distribution with variance matrix Q_{tt}. Therefore, the misclosure vector $\underline{t}$ and its known distribution under $\mathcal{H}_0$ form the basis of any statistical testing procedure.

A testing procedure can be defined by unambiguously mapping the outcomes of $\underline{t}$ to the hypotheses $\mathcal{H}_i$ for $i = 0, \ldots, k$. This is achieved by partitioning the misclosure space $\mathbb{R}^r$ into $k+1$ disjoint regions $\mathcal{P}_i \subset \mathbb{R}^r$ for $i = 0, \ldots, k$. Consequently, the testing procedure can be described as follows (Teunissen 2018)

$$\text{select } \mathcal{H}_i \text{ if and only if } \underline{t} \in \mathcal{P}_i, \ \text{for } i = 0, \ldots, k \tag{4}$$

The above representation of testing decisions enables the formulation of the final outcome of the DIA method, namely the *DIA-estimator*, in a single equation (see 7).

2.3 DIA-estimator

The decision of the testing process determines how the unknown parameter vector x should be estimated. If the outcome of testing is the acceptance of $\mathcal{H}_0$, i.e. $\underline{t} \in \mathcal{P}_0$, then x will get estimated based on (1). The Best Linear Unbiased Estimator (BLUE) of x under $\mathcal{H}_0$ is given by

$$\underline{\hat{x}}_0 = A^+ \underline{y} \tag{5}$$

where $A^+ = Q_{\hat{x}_0\hat{x}_0} A^T Q_{yy}^{-1}$ is the BLUE-inverse of A with $Q_{\hat{x}_0\hat{x}_0} = (A^T Q_{yy}^{-1} A)^{-1}$ the variance matrix of $\underline{\hat{x}}_0$. Note that $\underline{\hat{x}}_0$ and $\underline{t}$ are statistically independent of each other under a given hypothesis. If the testing decision is to select the alternative hypothesis $\mathcal{H}_{i\neq 0}$, i.e. $\underline{t} \in \mathcal{P}_{i\neq 0}$, then $\underline{\hat{x}}_0$ should be adapted as

$$\underline{\hat{x}}_i = \underline{\hat{x}}_0 - A^+ C_i \underline{\hat{b}}_i, \quad i = 1, \ldots, k \tag{6}$$

where $\underline{\hat{b}}_i = C_{t_i}^+ \underline{t}$ is the BLUE of b_i under $\mathcal{H}_i$ with $C_{t_i}^+ = (C_{t_i}^T Q_{tt}^{-1} C_{t_i})^{-1} C_{t_i}^T Q_{tt}^{-1}$ the BLUE-inverse of C_{t_i}.

The actual estimator for x produced by the combined estimation-testing nature of the DIA method is the DIA-estimator (Teunissen 2018) which reads

$$\underline{\bar{x}} = \sum_{i=0}^{k} \underline{\hat{x}}_i \, p_i(\underline{t}) \tag{7}$$

with $p_i(t)$ the indicator function of $\mathcal{P}_i$, i.e. $p_i(t) = 1$ for $t \in \mathcal{P}_i$ and $p_i(t) = 0$ elsewhere. The probabilistic properties of the DIA-estimator can be captured by its Probability Density Function (PDF), which under the hypothesis $\mathcal{H}_{i\in[0,\ldots,k]}$ is characterized by (Teunissen 2018)

$$f_{\underline{\bar{x}}}(\theta|\mathcal{H}_i) = \sum_{j=0}^{k} f_{\underline{\hat{x}}_j|\underline{t}\in\mathcal{P}_j}(\theta|\underline{t} \in \mathcal{P}_j, \mathcal{H}_i)\mathsf{P}(\underline{t} \in \mathcal{P}_j|\mathcal{H}_i) \tag{8}$$

with $f_{\underline{\hat{x}}_j|\underline{t}\in\mathcal{P}_j}(\theta|\underline{t} \in \mathcal{P}_j, \mathcal{H}_i)$ the conditional PDF of $\underline{\hat{x}}_j$ conditioned on $\underline{t} \in \mathcal{P}_j$ under $\mathcal{H}_i$.

2.4 Bias-known case

For the case where the biases b_i (for $i = 1, \ldots, k$) are fully known, which is the focus of this contribution, the x-estimator under $\mathcal{H}_{i\neq 0}$ in (6) would change to

$$\underline{\hat{x}}_i = \underline{\hat{x}}_0 - A^+ C_i b_i, \quad i = 1, \ldots, k \tag{9}$$

which, in comparison with (6), replaces the BLUE of b_i with its known vector. We note that $\underline{\hat{x}}_i$ and $\underline{\hat{x}}_0$ have the same dispersion, but different expectations. Therefore, like $\underline{\hat{x}}_0$, *all* the

estimators $\hat{\underline{x}}_i$'s ($i = 1, \ldots, k$) in (9), are *independent* from the misclosure of the $\mathcal{H}_0$-model, $\underline{t}$, under a given hypothesis.

With (9), the DIA-estimator (7) can be written as

$$\bar{\underline{x}} = \hat{\underline{x}}_0 - A^+ \sum_{i=1}^{k} C_i b_i p_i(\underline{t}) \tag{10}$$

and its PDF is given by

$$f_{\bar{\underline{x}}}(\theta|\mathcal{H}_i) = \sum_{j=0}^{k} f_{\hat{\underline{x}}_0}(\theta + A^+ C_j b_j|\mathcal{H}_i)\mathsf{P}(\underline{t} \in \mathcal{P}_j|\mathcal{H}_i) \tag{11}$$

which is a weighted average of shifted versions of the PDF of $\hat{\underline{x}}_0$, $f_{\hat{\underline{x}}_0}(\theta|\mathcal{H}_i)$, over $A^+C_jb_j$ for $j = 0, \ldots, k$, where the weights are determined by the probabilities of the testing decisions. In the following, we work with the DIA-estimator (10) and its distribution in (11).

3 Misclosure space partitioning

The DIA-estimator (10) represents a class of estimators, each uniquely defined by its partitioning of the misclosure space. Altering the testing procedure changes this partitioning and, consequently, the DIA-estimator. In this section, we consider a few members of this class, where the misclosure-space partitionings are defined using the concept of *minimum mean penalty testing*.

3.1 Penalized testing

Teunissen (2024a) introduced penalized testing to provide a means for comparing the quality of different misclosure-space partitionings. In penalized testing, each testing decision, say $t \in \mathcal{P}_i$, is assigned a nonnegative risk penalizing function $r_{i\alpha}(t)$ for each of the $k+1$ hypotheses $\mathcal{H}_\alpha$ (for $\alpha = 0, \ldots, k$). Thus, the hypothesis $\mathcal{H}_\alpha$-penalty function can be written as

$$r_\alpha(t) = \sum_{i=0}^{k} r_{i\alpha}(t)\, p_i(t) \tag{12}$$

which is the penalty given when the sample outcome of the misclosure vector is t and hypothesis $\mathcal{H}_\alpha$ is true. Therefore, the penalty associated with the partitioning $\mathcal{P}_{i\in[0,\ldots,k]}$ is a random variable as it is driven by the outcome of $\underline{t}$ and $\underline{\mathcal{H}}$, both of which are random. The random risk penalty variable can be formulated as

$$\underline{r} = \sum_{\alpha=0}^{k} r_\alpha(\underline{t})\iota_\alpha(\underline{\mathcal{H}}) \tag{13}$$

with $\iota_\alpha(\mathcal{H})$ the indicator function of the hypothesis $\mathcal{H}_\alpha$, where $\iota_\alpha(\mathcal{H}) = 1$ if $\mathcal{H} = \mathcal{H}_\alpha$ and $\iota_\alpha(\mathcal{H}) = 0$ otherwise.

One can compare different testing procedures by looking at their *mean penalty*. With (13), the mean penalty, conditioned on either $\mathcal{H}_\alpha$ or t, reads

$$\begin{aligned} \mathsf{E}(\underline{r}|\mathcal{H}_\alpha) &= \int_{\mathbb{R}^r} r_\alpha(t)\, f_{\underline{t}}(t|\mathcal{H}_\alpha)\mathrm{d}t \\ \mathsf{E}(\underline{r}|t) &= \sum_{\alpha=0}^{k} r_\alpha(t)\mathsf{P}[\mathcal{H}_\alpha|t] \end{aligned} \tag{14}$$

and the unconditional mean penalty reads

$$\begin{aligned} \mathsf{E}(\underline{r}) &= \sum_{\alpha=0}^{k} \mathsf{E}(\underline{r}|\mathcal{H}_\alpha)\mathsf{P}[\mathcal{H}_\alpha] \\ &= \int_{\mathbb{R}^r} \mathsf{E}(\underline{r}|t)\, f_{\underline{t}}(t)\mathrm{d}t \end{aligned} \tag{15}$$

where

$$\mathsf{P}[\mathcal{H}_\alpha|t] = \frac{f_{\underline{t}}(t|\mathcal{H}_\alpha)\mathsf{P}[\mathcal{H}_\alpha]}{f_{\underline{t}}(t)} \tag{16}$$

and

$$f_{\underline{t}}(t) = \sum_{\alpha=0}^{k} f_{\underline{t}}(t|\mathcal{H}_\alpha)\mathsf{P}[\mathcal{H}_\alpha] \tag{17}$$

Substitution of the second equation of (14) into the second equation of (15) gives, after the use of (12),

$$\mathsf{E}(\underline{r}) = \sum_{i=0}^{k} \int_{\mathcal{P}_i} \sum_{\alpha=0}^{k} r_{i\alpha}(t)\mathsf{P}[\mathcal{H}_\alpha|t]\, f_{\underline{t}}(t)\mathrm{d}t \tag{18}$$

Note, with $\mathsf{E}(\underline{r})$ being the mean penalty, that $1 - \mathsf{E}(\underline{r})$ may be considered the mean *reward*. For a given set of penalty functions $r_{i\alpha}(t)$ (for $i, \alpha = 0, \ldots, k$), any change in the partitioning of $\mathbb{R}^r$ would result in a corresponding change in the mean penalty $\mathsf{E}(\underline{r})$ (or the mean reward). The misclosure-space partitioning that minimizes the mean penalty (or maximizes the mean reward) is given as (Teunissen, 2024a, Theorem 2a)

$$\begin{aligned} \mathcal{P}_{i\in[0,\ldots,k]} &= \arg \min_{\mathcal{P}_{j\in[0,\ldots,k]}} \mathsf{E}(\underline{r}) \\ &= \left\{ t \in \mathbb{R}^r \,\middle|\, i = \arg \min_{j\in[0,\ldots,k]} \sum_{\alpha=0}^{k} r_{j\alpha}(t)\mathsf{P}[\mathcal{H}_\alpha|t] \right\} \\ &= \left\{ t \in \mathbb{R}^r \,\middle|\, i = \arg \max_{j\in[0,\ldots,k]} \sum_{\alpha=0}^{k} [1 - r_{j\alpha}(t)]\mathsf{P}[\mathcal{H}_\alpha|t] \right\} \end{aligned} \tag{19}$$

In geodetic applications, $\mathcal{P}_0$ is usually determined through the OMT (Baarda 1968), based on a user-defined false alarm

probability. If $\mathcal{P}_0$ is known, then the $\mathcal{P}_0$-*constrained* counterpart of (19) is obtained by

$$\begin{aligned}\mathcal{P}_{i\in[1,\ldots,k]} &= \arg \min_{\mathcal{P}_{j\in[1,\ldots,k]}\in\mathbb{R}^r\setminus\mathcal{P}_0} \mathsf{E}(\underline{r}) \\ &= \arg \min_{\mathcal{P}_{j\in[1,\ldots,k]}\in\mathbb{R}^r\setminus\mathcal{P}_0} \sum_{i=1}^{k}\int_{\mathcal{P}_i}\sum_{\alpha=0}^{k} r_{i\alpha}(t)\mathsf{P}[\mathcal{H}_\alpha|t]f_{\underline{t}}(t)\mathrm{d}t \\ &= \left\{ t\in\mathbb{R}^r\setminus\mathcal{P}_0 \middle| i = \arg\min_{j\in[1,\ldots,k]}\sum_{\alpha=0}^{k} r_{j\alpha}(t)\mathsf{P}[\mathcal{H}_\alpha|t]\right\} \\ &= \left\{ t\in\mathbb{R}^r\setminus\mathcal{P}_0 \middle| i = \arg\max_{j\in[1,\ldots,k]}\sum_{\alpha=0}^{k} [1-r_{j\alpha}(t)]\mathsf{P}[\mathcal{H}_\alpha|t]\right\}\end{aligned} \tag{20}$$

From the second equality, it is clear that the partitioning (20) minimizes only a part of the mean penalty $\mathsf{E}(\underline{r})$. As a result, the $\mathcal{P}_0$-constrained partitioning incurs a larger penalty compared to its unconstrained counterpart in (19).

We note that the above partitioning or its $\mathcal{P}_0$-constrained variant, given (16) and (17), is only applicable when the PDFs $f_{\underline{t}}(t|\mathcal{H}_\alpha)$ for $\alpha = 0,\ldots,k$ are completely known. In general, however, the bias vectors b_α associated with $\mathcal{H}_\alpha$ are not known, and thus one can only work with these PDFs conditioned on a given bias vector. In that case, one can work with the BLUEs of the bias vectors to estimate the mean penalty which can be shown to be an upper bound for the actual mean penalty (Teunissen 2024a). If all the bias vectors are known, these PDFs are fully determined, allowing the partitionings (19) and (20) to be applied directly.

Different choices of penalty functions lead to different minimum mean penalty partitionings of the misclosure space. In the following, we consider three such choices, which result in the following partitionings: I) representing the traditional DIA procedure commonly used in geodetic applications; II) maximizing probability of correct hypothesis identification; and III) maximizing probability of correct parameter estimation.

3.2 Traditional DIA

When the biases $b_{i\in[1,\ldots,k]}$ are unknown, a traditional geodetic approach for testing combines the OMT (Baarda 1968) with likelihood-ratio-based tests (Teunissen 2024b) to select the most likely hypothesis. The detection and identification of such approach can be summarized as follows. In the detection step, the OMT is used to validate the null hypothesis, whereby $\mathcal{H}_0$ is accepted if the outcome of $\underline{t}$ lies in

$$\mathcal{P}_0^{\mathrm{I}} = \left\{ t\in\mathbb{R}^r \middle| S_0^{\mathrm{I}} \le \chi^2_{1-\mathsf{P}_{\mathrm{FA}}}(r,0)\right\} \tag{21}$$

in which S_0^{I} is a realization of

$$\underline{S}_0^{\mathrm{I}} = \|\underline{t}\|^2_{Q_{tt}} \tag{22}$$

and $\chi^2_{1-\mathsf{P}_{\mathrm{FA}}}(r,0)$ is the $(1-\mathsf{P}_{\mathrm{FA}})$ quantile of the central Chi-square distribution with r degrees of freedom, and P_{FA} is the probability of false alarm, typically set a priori by the user. Since $\mathcal{H}_0$ is the working hypothesis one believes in, one will want to work with a sufficiently large acceptance region for the null hypothesis $\mathcal{H}_0$, i.e. a large $\mathcal{P}_0^{\mathrm{I}}$. Therefore, P_{FA} is usually set to small values.

Upon the rejection of $\mathcal{H}_0$ in the detection step, one moves to the identification step, where the most likely alternative hypothesis is chosen using

$$\underline{S}^{\mathrm{I}}_{i\in[1,\ldots,k]} = \|\underline{\hat{e}}_i\|^2_{Q_{yy}} \tag{23}$$

with $\underline{\hat{e}}_i$ the least-squares residual vector of the $\mathcal{H}_i$-model, which, in the bias-known case, takes the form $\underline{\hat{e}}_i = \underline{y} - A\,\underline{\hat{x}}_i - C_i b_i$. Selecting the hypothesis with the smallest realization of $\underline{S}^{\mathrm{I}}_{i\in[1,\ldots,k]}$, leads to the selection of the best-fitting model among the considered alternative hypotheses. The above test statistic can also be formulated in the $\mathcal{H}_0$-model misclosure as

$$\underline{S}^{\mathrm{I}}_{i\in[1,\ldots,k]} = \|\underline{t} - C_{t_i} b_i\|^2_{Q_{tt}} \tag{24}$$

Therefore, the alternative hypothesis $\mathcal{H}_{i\in[1,\ldots,k]}$ is selected as the most likely hypothesis if the outcome of $\underline{t}$ lies in

$$\mathcal{P}^{\mathrm{I}}_{i\in[1,\ldots,k]} = \left\{ t\in\mathbb{R}^r\setminus\mathcal{P}_0^{\mathrm{I}} \middle| i = \arg\min_{j\in[1,\ldots,k]} S_j^{\mathrm{I}}\right\} \tag{25}$$

One can easily verify that the regions (21) and (25) together cover the entire misclosure space $\mathbb{R}^r$. Any $t \in \mathbb{R}^r\setminus\mathcal{P}_0^{\mathrm{I}}$ produces a vector of k realizations $S^{\mathrm{I}}_{i\in[1,\ldots,k]}$ as defined by (24). For any such t, there exists a region $\mathcal{P}_i^{\mathrm{I}}$ containing it, for some $i \in \{1,\ldots,k\}$. Hence, $\bigcup_{i=0}^k \mathcal{P}_i^{\mathrm{I}} = \mathbb{R}^r$. In order for the regions (21) and (25) to form a partitioning of the misclosure space, they must also be mutually disjoint, i.e. $\mathcal{P}_i^{\mathrm{I}} \cap \mathcal{P}_j^{\mathrm{I}} = \emptyset$ for any $i \neq j$. As $\mathcal{P}^{\mathrm{I}}_{i\in[1,\ldots,k]}$ are defined in $\mathbb{R}^r\setminus\mathcal{P}_0^{\mathrm{I}}$, they are all disjoint from $\mathcal{P}_0^{\mathrm{I}}$. For the mutual disjointness of $\mathcal{P}^{\mathrm{I}}_{i\neq0}$ and $\mathcal{P}^{\mathrm{I}}_{j\neq0}$, we have the following result.

Lemma 1 *Consider the regions in (25). For any $i \neq j$, $\mathcal{P}_i^{\mathrm{I}} \cap \mathcal{P}_j^{\mathrm{I}} = \emptyset$ if and only if $C_i b_i - C_j b_j \neq Av$ for all $v \in \mathbb{R}^n$.*

Proof See 'Appendix'. □

To show how the above partitioning can be obtained based on $\mathcal{P}_0$-constrained minimization of the mean penalty, we make use of the following Lemma.

Lemma 2 *Let the misclosure vector be normally distributed (cf. 3). Further, assume that all the alternative hypotheses have the same probability of occurrence, i.e.* $\mathsf{P}[\mathcal{H}_1] = \ldots = \mathsf{P}[\mathcal{H}_k]$*, and that the penalty function is chosen such that*

$$r_{j\alpha}(t) = 1 - \delta_{j\alpha} \tag{26}$$

with $\delta_{j\alpha}$ *the Kronecker delta. Under these assumptions, the* $\mathcal{P}_0$*-constrained partitioning (20) simplifies to*

$$\mathcal{P}_{i\in[1,\ldots,k]} = \left\{ t \in \mathbb{R}^r \setminus \mathcal{P}_0 \,\middle|\, i = \arg \min_{j\in[1,\ldots,k]} S^{\mathrm{I}}_j \right\} \tag{27}$$

□

Proof Incorporating the penalty function (26), the objective function in (20) is expressed as $\sum_{\alpha=0}^{k}[1 - r_{j\alpha}(t)]\mathsf{P}[\mathcal{H}_\alpha|t] = \mathsf{P}[\mathcal{H}_j|t]$. Using (16), and under the assumptions that all alternative hypotheses have the same probability of occurrence and that the misclosure vector is normally distributed, (27) follows. □

It can be easily seen that (25) is a special case of (27) where $\mathcal{P}_0 = \mathcal{P}^{\mathrm{I}}_0$. Therefore, if all correct decisions are assigned a zero penalty and the penalties for incorrect decisions are set to one, then the misclosure space partitioning induced by the traditional DIA method would be a $\mathcal{P}_0$-constrained minimum mean penalty partitioning, provided that all the alternative hypotheses are equally likely.

3.3 Maximizing probability of correct hypothesis identification

The assumption that all alternative hypotheses have the same probability of occurrence might not be valid for all applications. Recognizing the difference in the likelihood of occurrence of different hypotheses, and incorporating the penalty function (26), the objective function in (19) is expressed as $\sum_{\alpha=0}^{k}[1 - r_{j\alpha}(t)]\mathsf{P}[\mathcal{H}_\alpha|t] = \mathsf{P}[\mathcal{H}_j|t]$. Consequently, the corresponding minimum mean penalty partitioning regions, without imposing any constraint on $\mathcal{P}_0$, are given by

$$\mathcal{P}^{\mathrm{II}}_{i\in[0,\ldots,k]} = \left\{ t \in \mathbb{R}^r \,\middle|\, i = \arg \max_{j\in[0,\ldots,k]} \mathsf{P}[\mathcal{H}_j|t] \right\} \tag{28}$$

with the maximum reward being the probability sum of correct hypothesis identifications,

$$1 - \min_{\mathcal{P}_j} \mathsf{E}(\underline{r}) = \max_{\mathcal{P}_j} \sum_{i=0}^{k} \mathsf{P}(\underline{t} \in \mathcal{P}_i, \mathcal{H}_i) \tag{29}$$

If one would like to have the acceptance region of $\mathcal{H}_0$ determined by the overall model test, i.e. $\mathcal{P}^{\mathrm{II}}_0 = \mathcal{P}^{\mathrm{I}}_0$ (cf. 21), then it follows that $\mathcal{P}^{\mathrm{I}}_{i\in[1,\ldots,k]}$ becomes a special case of $\mathcal{P}^{\mathrm{II}}_{i\in[1,\ldots,k]}$. Furthermore, the two partitionings would be identical if, in addition, $\mathsf{P}[\mathcal{H}_1] = \ldots = \mathsf{P}[\mathcal{H}_k]$.

Using (3) and (16), the partitioning (28) simplifies to

$$\mathcal{P}^{\mathrm{II}}_{i\in[0,\ldots,k]} = \left\{ t \in \mathbb{R}^r \,\middle|\, i = \arg \min_{j\in[0,\ldots,k]} S^{\mathrm{II}}_j \right\} \tag{30}$$

where

$$S^{\mathrm{II}}_j = S^{\mathrm{I}}_j - \ln[\mathsf{P}[\mathcal{H}_j]^2] \tag{31}$$

The testing procedure corresponding with these partitioning regions selects, among all the considered hypotheses, the one that has the best fit to the observed data while having a higher probability of occurrence.

Similar to $\mathcal{P}^{\mathrm{I}}_{i\in[0,\ldots,k]}$, it can be shown that the regions $\mathcal{P}^{\mathrm{II}}_{i\in[0,\ldots,k]}$ also cover the whole misclosure space $\mathbb{R}^r$, i.e. $\bigcup_{i=0}^{k} \mathcal{P}^{\mathrm{II}}_i = \mathbb{R}^r$. The following Lemma presents the necessary and sufficient condition for $\mathcal{P}^{\mathrm{II}}_i$ and $\mathcal{P}^{\mathrm{II}}_j$, with $i \neq j$, to be disjoint, so that $\mathcal{P}^{\mathrm{II}}_{i\in[0,\ldots,k]}$ form a partitioning of $\mathbb{R}^r$.

Lemma 3 *Consider the regions in (30). For any* $i \neq j$*, with* $C_0 b_0 = 0$*,* $\mathcal{P}^{\mathrm{II}}_i \cap \mathcal{P}^{\mathrm{II}}_j = \emptyset$ *if and only if at least one of the following holds:*

(1) $C_i b_i - C_j b_j \neq Av$ *for all* $v \in \mathbb{R}^n$*;*

(2) $\mathsf{P}[\mathcal{H}_i] \neq \mathsf{P}[\mathcal{H}_j]$.

Proof See 'Appendix'. □

Note that $\mathcal{H}_0$ is often significantly more likely to occur compared to the alternative hypotheses, i.e. $\mathsf{P}[\mathcal{H}_0] >> \mathsf{P}[\mathcal{H}_{i\neq 0}]$. Furthermore, $C_0 b_0 = 0$ and $C_i b_i \neq 0$ for any $i \neq 0$. Together with the assumption that $[A\ C_i]$ is a full-rank matrix, this implies that both (1) and (2) hold for $i = 0 \neq j$. Therefore, $\mathcal{P}^{\mathrm{II}}_0$ is disjoint from any $\mathcal{P}^{\mathrm{II}}_{j\neq 0}$. Moreover, if (1) does not hold for some $i \neq j$, while $\mathsf{P}[\mathcal{H}_i] > \mathsf{P}[\mathcal{H}_j]$, then $\mathcal{P}^{\mathrm{II}}_j = \emptyset$. This happens as both $\mathcal{H}_i$ and $\mathcal{H}_j$ have the same fit to the observed data, but $\mathcal{H}_j$ is always penalized relative to $\mathcal{H}_i$ due to its lower probability of occurrence. Finally, we remark that the above Lemma also applies when $\mathcal{P}^{\mathrm{II}}_0$ is constrained, e.g. $\mathcal{P}^{\mathrm{II}}_0 = \mathcal{P}^{\mathrm{I}}_0$.

3.4 Maximizing probability of correct parameter estimation

In the previous subsection, it was demonstrated how a certain choice of penalty function yields a partitioning maximizing the probability of correct decisions. While this property is appealing from a *testing* perspective, it may not be adequate from an *estimation* standpoint. Let us assume that it is desirable for the DIA-estimator to lie in the x-centered 'safety'

region $\Omega_x \subset \mathbb{R}^n$. If the penalty function is chosen such that (Teunissen 2024a)

$$r_{j\alpha}(t) = \mathsf{P}(\underline{\hat{x}}_j \notin \Omega_x | \mathcal{H}_\alpha, t) \tag{32}$$

then, the corresponding minimum mean penalty partitioning is given by

$$\mathcal{P}^{\mathrm{III}}_{i\in[0,\ldots,k]} = \left\{ t \in \mathbb{R}^r \middle| i = \arg \max_{j\in[0,\ldots,k]} \mathsf{P}(\underline{\hat{x}}_j \in \Omega_x | t) \right\} \tag{33}$$

with the maximum reward being the probability of the DIA-estimator residing in Ω_x,

$$1 - \min_{\mathcal{P}_j} \mathsf{E}(\underline{r}) = \max_{\mathcal{P}_j} \mathsf{P}(\underline{\bar{x}} \in \Omega_x) \tag{34}$$

Therefore, the choice of (32) as the penalty function yields the DIA estimator that, within its class, has the highest probability of lying inside its safety region.

When the biases are known, as (9) shows, all the estimators $\underline{\hat{x}}_{i\in[0,\ldots,k]}$ are independent from $\underline{t}$ under a given hypothesis. Therefore, the conditioning on $\underline{t} = t$ of the probability in (32) would disappear, so does the dependency of the penalty function on t. In this instance, for the special case of ellipsoidal safety regions where

$$\Omega_x = \left\{ u \in \mathbb{R}^n \middle| \|u - x\|^2_{Q_{\hat{x}_0\hat{x}_0}} \leq \tau^2 \right\} \tag{35}$$

the penalty function in (32) specializes to

$$r_{j\alpha} = \mathsf{P}[\underline{\chi}^2(n, \lambda_{j\alpha}) > \tau^2] \tag{36}$$

with $\underline{\chi}^2(n, \lambda)$ a random variable with a non-central Chi-square distribution with n degrees of freedom and non-centrality parameter λ, and

$$\lambda_{j\alpha} = \|A^+[C_j b_j - C_\alpha b_\alpha]\|^2_{Q_{\hat{x}_0\hat{x}_0}} \tag{37}$$

with $C_0 b_0 = 0$. The partitioning (33) for the penalty function (36) can be formulated, using (3), as

$$\mathcal{P}^{\mathrm{III}}_{i\in[0,\ldots,k]} = \left\{ t \in \mathbb{R}^r \middle| i = \arg \max_{j\in[0,\ldots,k]} S^{\mathrm{III}}_j \right\} \tag{38}$$

where

$$S^{\mathrm{III}}_j = \sum_{\alpha=0}^{k} \mathsf{P}[\underline{\chi}^2(n, \lambda_{j\alpha}) \leq \tau^2] \exp\left\{ -\frac{1}{2} S^{\mathrm{II}}_\alpha \right\} \tag{39}$$

The regions $\mathcal{P}^{\mathrm{III}}_{i\in[0,\ldots,k]}$, similar to (30), cover the whole misclosure space $\mathbb{R}^r$, i.e. $\bigcup_{i=0}^k \mathcal{P}^{\mathrm{III}}_i = \mathbb{R}^r$. However, unlike the two previous partitionings, deriving the necessary and sufficient condition for $\mathcal{P}^{\mathrm{III}}_i$ and $\mathcal{P}^{\mathrm{III}}_j$, with $i \neq j$, to be disjoint—thereby ensuring that $\mathcal{P}^{\mathrm{III}}_{i\in[0,\ldots,k]}$ partition $\mathbb{R}^r$—is not straightforward. Nonetheless, it is easy to verify that if $A^+C_i b_i = A^+C_j b_j$, or alternatively $C_i b_i - C_j b_j = Q_{yy}Bu$ for some $u \in \mathbb{R}^r$, then $\lambda_{i\alpha} = \lambda_{j\alpha}$ for all $\alpha \in [0, \ldots, k]$. Consequently, $S^{\mathrm{III}}_i = S^{\mathrm{III}}_j$, implying that $\mathcal{P}^{\mathrm{III}}_i = \mathcal{P}^{\mathrm{III}}_j$. This is also the case for the $\mathcal{P}_0$-constrained variant of (38).

Table 1 summarizes the three partitionings discussed above, along with the required user inputs necessary for their application.

4 Performance comparison of DIA-estimators

In this section, we compare the three partitionings (21) +(25), (30), and (38) along with their corresponding DIA-estimators through a series of bias-known examples. Our analysis also incorporates the $\mathcal{P}_0$-constrained versions of (30) and (38), where their $\mathcal{H}_0$ acceptance region is constrained to be the same as $\mathcal{P}^{\mathrm{I}}_0$. In these examples, we assume $\mathsf{P}[\mathcal{H}_1] = \ldots = \mathsf{P}[\mathcal{H}_k]$, making the $\mathcal{P}_0$-constrained version of (30) identical to (25), as $S^{\mathrm{II}}_i - S^{\mathrm{II}}_j = S^{\mathrm{I}}_i - S^{\mathrm{I}}_j$ for any $i, j \neq 0$. We denote the $\mathcal{P}_0$-constrained version of (38) as $\mathcal{P}^{\mathrm{IV}}_{i\in[0,\ldots,k]}$. The DIA-estimators yielded by these partitionings are denoted by $\underline{\bar{x}}^\iota$ with $\iota = \mathrm{I}, \ldots, \mathrm{IV}$.

We begin with a simple example to illustrate the differences between these partitionings, which helps establish a clear foundation for understanding. Building on the insights gained from this example, we then consider more practical examples in the context of terrestrial surveying.

4.1 Simple example

Let $\underline{y} \in \mathbb{R}^3$ contain three equally-precise repeat measurements of the unknown quantity $x \in \mathbb{R}$, which implies $A = e_3$ and $Q_{yy} = \sigma^2 I_3$ with σ the standard deviation of the individual observables. Three alternative hypotheses are put forward, each addressing the presence of a known bias in a different observable, and thus $C_i = c_i \in \mathbb{R}^3$ $(i = 1, 2, 3)$ are canonical unit vectors and $b_i \in \mathbb{R}$ $(i = 1, 2, 3)$ are scalars. In this case, if $b_i = b_j$ for $i \neq j$, then, since $A^+ = \frac{1}{3}e_3^T$, we have $A^+c_i = A^+c_j$. Consequently, $\mathcal{P}^{\mathrm{III}}_i = \mathcal{P}^{\mathrm{III}}_j$ and also $\mathcal{P}^{\mathrm{IV}}_i = \mathcal{P}^{\mathrm{IV}}_j$ for $i, j = 1, 2, 3$. To avoid this non-separability of the alternative hypotheses, we assume different values for each b_i. The three alternatives are assumed to be equally likely, i.e. $\mathsf{P}[\mathcal{H}_i] = (1 - \mathsf{P}[\mathcal{H}_0])/3$ for $i = 1, 2, 3$.

4.1.1 Misclosure space partitioning

Assuming $\sigma = 1$, Fig. 1 illustrates (21)+(25) with $\mathsf{P}_{\mathrm{FA}} = 0.01$; Fig. 2 illustrates (30); and Fig. 3 illustrates (38) along

Table 1 An overview of the misclosure space partitioning regions studied in this contribution

Misclosure Space Partitioning	User Input	Property
$\mathcal{P}_0^{\mathrm{I}} = \left\{ t \in \mathbb{R}^r \,\middle|\, S_0^{\mathrm{I}} \le \chi^2_{1-\mathsf{P}_{\mathrm{FA}}}(r,0) \right\}$	P_{FA}	Traditional DIA
$\mathcal{P}_{i\in[1,\ldots,k]}^{\mathrm{I}} = \left\{ t \in \mathbb{R}^r \setminus \mathcal{P}_0^{\mathrm{I}} \,\middle|\, i = \arg\min_{j\in[1,\ldots,k]} S_j^{\mathrm{I}} \right\}$ with $\underline{S}_0^{\mathrm{I}} = \|\underline{t}\|^2_{Q_{tt}}$ and $\underline{S}_{j\neq 0}^{\mathrm{I}} = \|\underline{t} - C_{t_j} b_j\|^2_{Q_{tt}}$		
$\mathcal{P}_{i\in[0,\ldots,k]}^{\mathrm{II}} = \left\{ t \in \mathbb{R}^r \,\middle|\, i = \arg\min_{j\in[0,\ldots,k]} S_j^{\mathrm{II}} \right\}$ with $S_j^{\mathrm{II}} = S_j^{\mathrm{I}} - \ln[\mathsf{P}[\mathcal{H}_j]^2]$	$\mathsf{P}[\mathcal{H}_i]$ for $i = 0,\ldots,k$	Maximizing $\sum_{i=0}^k \mathsf{P}(\underline{t} \in \mathcal{P}_i, \mathcal{H}_i)$
$\mathcal{P}_{i\in[0,\ldots,k]}^{\mathrm{III}} = \left\{ t \in \mathbb{R}^r \,\middle|\, i = \arg\max_{j\in[0,\ldots,k]} S_j^{\mathrm{III}} \right\}$ with $S_j^{\mathrm{III}} = \sum_{\alpha=0}^{k} \mathsf{P}[\underline{\chi}^2(n,\lambda_{j\alpha}) \le \tau^2] \exp\{-\frac{1}{2} S_\alpha^{\mathrm{II}}\}$ and $\lambda_{j\alpha} = \|A^+[C_j b_j - C_\alpha b_\alpha]\|^2_{Q_{\hat{x}_0\hat{x}_0}}$	$\mathsf{P}[\mathcal{H}_i]$ for $i = 0,\ldots,k$	Maximizing $\mathsf{P}(\underline{\hat{x}} \in \Omega_x)$ with $\Omega_x = \left\{ u \in \mathbb{R}^n \,\middle|\, \|u - x\|^2_{Q_{\hat{x}_0\hat{x}_0}} \le \tau^2 \right\}$

with its $\mathcal{P}_0$-constrained version setting $\mathsf{P}_{\mathrm{FA}} = 0.01$. These figures correspond to the above example for different sets of biases $b = [b_1,\ b_2,\ b_3]$. The partitioning regions are shown in different shades of gray, getting darker as i increases from 0 to 3. Note that the misclosure vector is formed by

$$B = \frac{1}{2\sqrt{3}} \begin{bmatrix} -2 & -2 \\ 1+\sqrt{3} & 1-\sqrt{3} \\ 1-\sqrt{3} & 1+\sqrt{3} \end{bmatrix} \tag{40}$$

which has identity matrix as its variance matrix, i.e. $Q_{tt} = I_2$. The geometry of partitionings will change, would one use a different B matrix from (40).

As the design matrix A is a vector of ones and all measurements are assumed to be equally precise, the angles between c_{t_i}'s are 120°. Consequently, the partitioning regions $\mathcal{P}_{i\in[1,2,3]}^{\mathrm{I}}$ would have identical shapes and sizes if $b_1 = b_2 = b_3$. However, as shown in Fig. 1, the biases under the alternative hypotheses have different values, resulting in $\mathcal{P}_{i\in[1,2,3]}^{\mathrm{I}}$ having different sizes and shapes. It can be seen that the common boundary between $\mathcal{P}_0^{\mathrm{I}}$ and $\mathcal{P}_{i\neq 0}^{\mathrm{I}}$ shrinks as b_i gets larger relative to the other biases. This occurs because the distance between a point t on the boundary of $\mathcal{P}_0^{\mathrm{I}}$ and $c_{t_i} b_i$ gets larger with larger b_i, reducing the number of points t on the boundary of $\mathcal{P}_0^{\mathrm{I}}$ that satisfy the inequality $S_i^{\mathrm{I}} < S_{j\neq i}^{\mathrm{I}}$. For instance, in the right panel, where $b = [5,\ 10,\ 20]$, $\mathcal{P}_0^{\mathrm{I}}$ shares no common boundary with $\mathcal{P}_3^{\mathrm{I}}$ since $c_{t_3} b_3$, among $c_{t_i} b_i$ for $i = 1, 2, 3$, is significantly farther from the points on the boundary of $\mathcal{P}_0^{\mathrm{I}}$.

In Fig. 2, comparing the left and middle panels with the right panel, we observe an expansion in $\mathcal{P}_0^{\mathrm{II}}$, which can be explained as follows. As (30) and (31) show, $\mathcal{P}_0^{\mathrm{II}}$ is formed by the intersection of k hyperplanes (lines in the 2D case) whose normal vectors are $c_{t_\alpha}, \alpha = 1,\ldots,k$, when $Q_{tt} = I_r$, as is the case with the example at hand. The distance from the origin to these hyperplanes is determined by $0.5\|c_{t_\alpha} b_\alpha\| + \frac{\ln \mathsf{P}[\mathcal{H}_0] - \ln \mathsf{P}[\mathcal{H}_i]}{\|c_{t_\alpha} b_\alpha\|}$. For $b_\alpha \in \mathbb{R}^+$, this distance is an increasing function of b_α if $b_\alpha \ge \frac{\sqrt{\ln[\mathsf{P}[\mathcal{H}_0]^2] - \ln[\mathsf{P}[\mathcal{H}_i]^2]}}{\|c_{t_\alpha}\|}$, which leads to the enlargement of the volume of $\mathcal{P}_0^{\mathrm{II}}$. Note that the boundary between regions $\mathcal{P}_{i\neq 0}^{\mathrm{II}}$ and $\mathcal{P}_{j\neq 0}^{\mathrm{II}}$, for $i,\ j = 1, 2, 3$, in Fig. 2 and the boundary between $\mathcal{P}_{i\neq 0}^{\mathrm{I}}$ and $\mathcal{P}_{j\neq 0}^{\mathrm{I}}$ in Fig. 1 , lie on the same hyperplane. This is due to the assumption in the current example that $\mathsf{P}[\mathcal{H}_i] = \mathsf{P}[\mathcal{H}_j]$.

Comparing the panels from left to right in Fig. 3 (excluding the last row), it is observed that the partitioning regions $\mathcal{P}_{\alpha\in[0,\ldots,k]}^{\mathrm{III}}$ approach in shape to $\mathcal{P}_{\alpha\in[0,\ldots,k]}^{\mathrm{II}}$ when the biases and their differences increase, which can be explained as follows. For the three-dimensional example at hand, since $A^+ c_j = \frac{1}{3}$, larger values of $|b_j - b_\alpha|$ for $j \neq \alpha$ lead to larger values of $\lambda_{j\alpha}$ (cf. 37). When $\lambda_{j\alpha}$ is much larger compared to τ^2, then $\mathsf{P}[\underline{\chi}^2(n,\lambda_{j\alpha}) \le \tau^2] \to 0$ and thus $S_j^{\mathrm{III}} \to \mathsf{P}[\underline{\chi}^2(n,0) \le \tau^2] \exp\{-\frac{1}{2} S_j^{\mathrm{II}}\}$. As a result, the maximization problem in (38) reduces to the minimization problem in (30), hence the similarity between $\mathcal{P}_{\alpha\in[0,\ldots,k]}^{\mathrm{III}}$ and $\mathcal{P}_{\alpha\in[0,\ldots,k]}^{\mathrm{II}}$ for large biases and bias differences.

By comparing the panels in the first and second rows of Fig. 3, we observe that as $\mathsf{P}[\mathcal{H}_0]$ increases from 0.9 to 0.99, $\mathcal{P}_0^{\mathrm{III}}$ expands in size. This outcome aligns with our expectations that a higher probability of the null hypothesis corresponds to a larger acceptance region, eventually leading to no rejection in the limit as $\mathsf{P}[\mathcal{H}_0] \to 1$. Furthermore, looking at the first and the third rows, we note that increasing τ^2 from 0.5 to 10, i.e. increasing the volume of Ω_x, reduces the size of $\mathcal{P}_0^{\mathrm{III}}$. This happens as enlarging the desirable region Ω_x makes the probability constraint on the DIA-estimator more relaxed so that a more frequent selec-

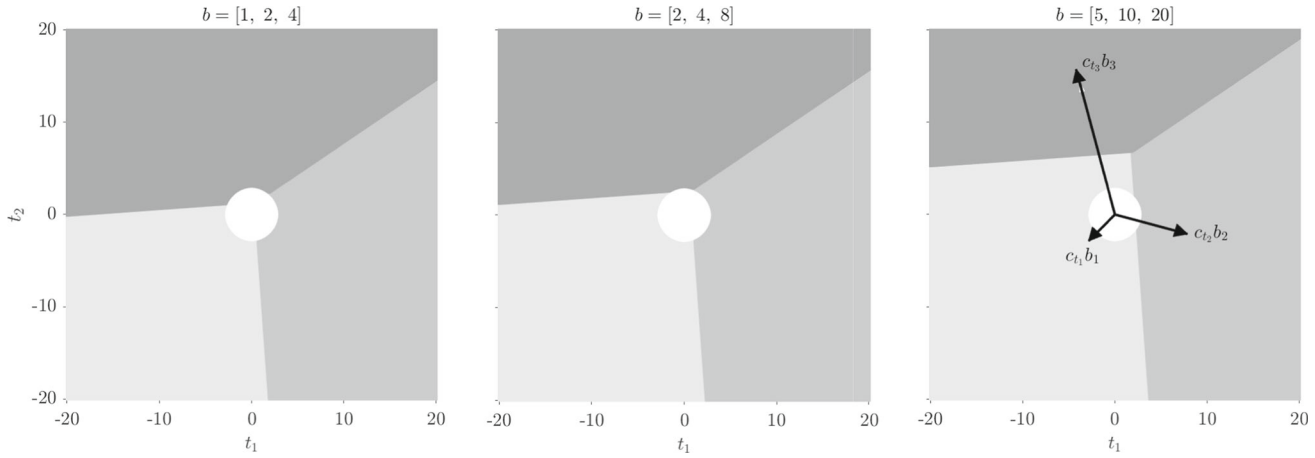

Fig. 1 Misclosure space partitioning corresponding with the simple example for traditional DIA (cf. 21 and 25) assuming $\sigma = 1$ and $\mathsf{P}_{\mathrm{FA}} = 0.01$. The partitioning regions $\mathcal{P}^{\mathrm{I}}_{i\in[0,\ldots,3]}$ are shown in different shades of gray, getting darker as i increases from 0 to 3. The panels from left to right correspond to different sets of biases $b = [b_1,\ b_2,\ b_3]$, as indicated at the top of each panel. The projection of observation bias vectors onto the misclosure space is shown in the right panel

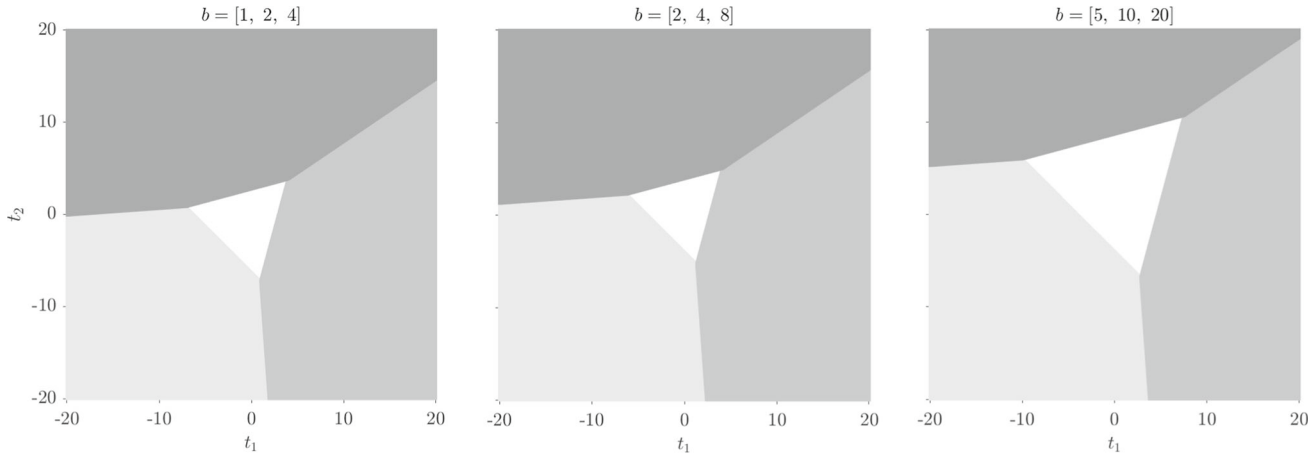

Fig. 2 Misclosure space partitioning corresponding with the simple example for maximizing probability of correct hypothesis identification (cf. 30) assuming $\sigma = 1$ and $\mathsf{P}[\mathcal{H}_0] = 0.9$. The partitioning regions $\mathcal{P}^{\mathrm{II}}_{i\in[0,\ldots,3]}$ are shown in different shades of gray, getting darker as i increases from 0 to 3. The panels from left to right correspond to different sets of biases $b = [b_1,\ b_2,\ b_3]$, as indicated at the top of each panel

tion of the alternatives, even though $\mathcal{H}_0$ is highly likely to be the true hypothesis, would still results in acceptable solutions for x. A comparison between the first and last row reveals, upon constraining $\mathcal{P}_0$, that $\mathcal{P}^{\mathrm{III}}_0 \setminus \mathcal{P}^{\mathrm{IV}}_0$ is predominantly inherited by $\mathcal{H}_1$, which, among the alternative hypotheses, has the smallest bias value.

Finally, we note that when the penalties change from $\{0, 1\}$ to $\mathsf{P}[\underline{\chi}^2(n, \lambda_{j\alpha}) > \tau^2]$, the geometry of the partitioning regions can change to the extent that some regions may leak between two adjacent areas, rendering them non-adjacent. For example, compare the left panels in Fig. 2 and the third row of Fig. 3. To further illustrate this difference, Fig. 4 [top] shows the latter, superimposed with the borders of the former. The bottom panel presents the penalty matrix, rounded to three decimal places, corresponding to the colored partitioning, with each column representing the penalties for different testing decisions under $\mathcal{H}_\alpha$, where $\alpha = 0, \ldots, 3$ from left to right. Each column of the penalty matrix, from top to bottom, contains the penalties for selecting $\mathcal{H}_i$, where $i = 0, \ldots, 3$. It can be seen that the penalty for choosing $\mathcal{H}_1$ when $\mathcal{H}_0$ is true, or choosing $\mathcal{H}_0$ when $\mathcal{H}_1$ is true, is approximately 4 times and 40 times smaller than the penalties for choosing $\mathcal{H}_2$ and $\mathcal{H}_3$ when $\mathcal{H}_0$ is true, or choosing $\mathcal{H}_0$ when $\mathcal{H}_2$ and $\mathcal{H}_3$ is true, respectively. This explains why $\mathcal{P}^{\mathrm{III}}_0$ is fully encompassed by $\mathcal{P}^{\mathrm{III}}_1$, and shares no common borders with $\mathcal{P}^{\mathrm{III}}_2$ or $\mathcal{P}^{\mathrm{III}}_3$. In addition, the penalty for choosing $\mathcal{H}_1$

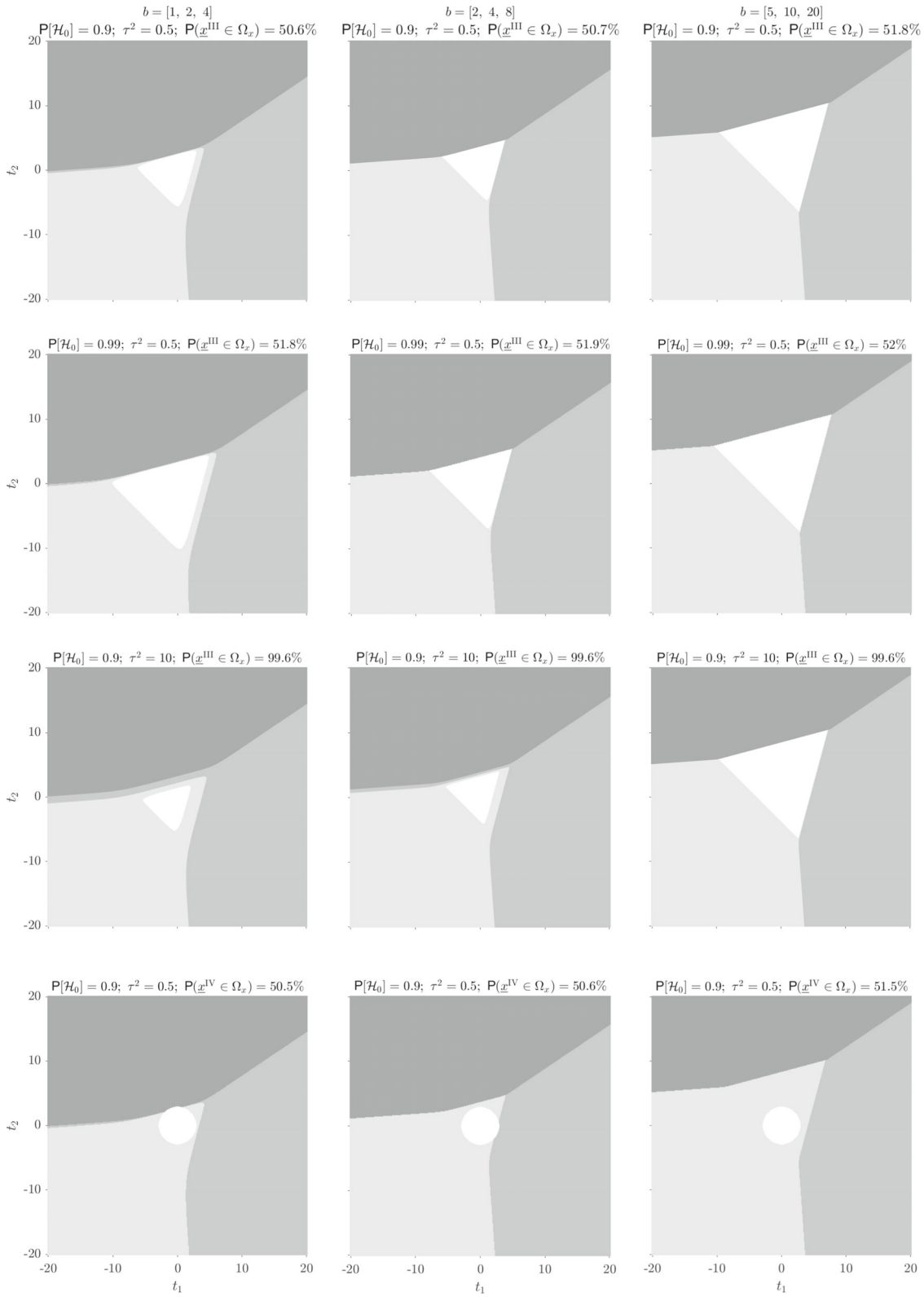

Fig. 3 Misclosure space partitioning corresponding with the simple example for maximizing probability of correct parameter estimation (cf. 38) assuming $\sigma = 1$. The last row shows the $\mathcal{P}_0$-constrained version of the top row setting $\mathsf{P}_{\mathrm{FA}} = 0.01$. The partitioning regions $\mathcal{P}^{\mathrm{III}}_{i\in[0,\ldots,3]}$ and $\mathcal{P}^{\mathrm{IV}}_{i\in[0,\ldots,3]}$ are shown in different shades of gray, getting darker as i increases from 0 to 3. The columns from left to right correspond to different sets of biases $b = [b_1,\ b_2,\ b_3]$, as indicated at the top of each column

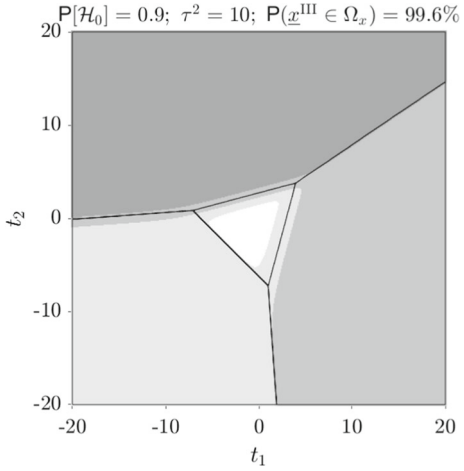

$$\begin{bmatrix} 0.002 & 0.005 & 0.022 & 0.197 \\ 0.005 & 0.002 & 0.005 & 0.076 \\ 0.022 & 0.005 & 0.002 & 0.022 \\ 0.197 & 0.076 & 0.022 & 0.002 \end{bmatrix}$$

Fig. 4 [Top] Illustration of the left panel in the third row of Fig. 3, superimposed with the borders of the left panel of Fig. 2. [Bottom] Penalty matrix corresponding to the colored partitioning, with each column representing the penalties for different testing decisions under $\mathcal{H}_\alpha$, where $\alpha = 0, \ldots, 3$ from left to right. Each column, from top to bottom, contains the penalties for selecting $\mathcal{H}_i$, where $i = 0, \ldots, 3$

under $\mathcal{H}_3$ (and vice versa) is 15 times higher than the penalty for choosing $\mathcal{H}_1$ under $\mathcal{H}_2$ (and vice versa). Consequently, $\mathcal{P}_2^{\text{III}}$ leaks between $\mathcal{P}_1^{\text{III}}$ and $\mathcal{P}_3^{\text{III}}$ due to the large harm associated with selecting $\mathcal{H}_1$ for misclosure vectors originating from $\mathcal{H}_3$.

4.1.2 DIA-estimator quality

The misclosure space partitionings $\mathcal{P}^\iota_{i\in[0,\ldots,k]}$ for $\iota \in \{\text{I}, \ldots, \text{IV}\}$ yield different DIA-estimators, denoted by $\underline{\bar{x}}^\iota$ for $\iota \in \{\text{I}, \ldots, \text{IV}\}$. Among these, $\underline{\bar{x}}^{\text{III}}$ has the highest probability of lying inside the user-specified safety region Ω_x, making it the *optimal* DIA-estimator from an estimation perspective. The quality of the other estimators can then be evaluated relative to $\underline{\bar{x}}^{\text{III}}$ by assessing their probabilities of falling within Ω_x.

Using the total probability rule, and given (35) and that the estimators $\underline{\hat{x}}_{i\in[0,\ldots,k]}$ in (9) are independent of $\underline{t}$ under $\mathcal{H}_{\alpha\in[0,\ldots,k]}$, one can write

$$\mathsf{P}(\underline{\bar{x}}^\iota \in \Omega_x) = \sum_{\alpha=0}^{k} \mathsf{P}[\mathcal{H}_\alpha] \sum_{i=0}^{k} \mathsf{P}[\underline{\chi}^2(n, \lambda_{i\alpha}) \le \tau^2] \mathsf{P}(\underline{t} \in \mathcal{P}_i^\iota | \mathcal{H}_\alpha) \tag{41}$$

While $\mathsf{P}[\underline{\chi}^2(n, \lambda_{i\alpha}) \le \tau^2]$ can be approximated using Chi-square distribution tables, see, e.g. (Haynam et al. 1982; Costa et al. 2010), the computation of $\mathsf{P}(\underline{t} \in \mathcal{P}_i^\iota | \mathcal{H}_\alpha)$ can be done through a Monte-Carlo simulation (Robert and Casella 2004). In doing so, we leverage the fact that probabilities can be expressed as expectations, and thus we have

$$\begin{aligned} \mathsf{P}(\underline{t} \in \mathcal{P}_i^\iota | \mathcal{H}_\alpha) &= \int_{\mathcal{P}_i^\iota} f_{\underline{t}}(\tau | \mathcal{H}_\alpha) \, \mathrm{d}\tau \\ &= \int_{\mathbb{R}^r} f_{\underline{t}}(\tau | \mathcal{H}_\alpha) \, p_i^\iota(\tau) \, \mathrm{d}\tau \\ &= \mathsf{E}(p_i^\iota(\underline{t}) | \mathcal{H}_\alpha) \end{aligned} \tag{42}$$

with $p_i^\iota(t)$ the indicator function of $\mathcal{P}_i^\iota$. The expectation in the last equality can be approximated by averaging a sufficient number of samples from the distribution. Let $t^{(s)} \in \mathbb{R}^r$, $s = 1, \ldots, N$, be sample vectors independently drawn from the distribution $f_{\underline{t}}(\tau | \mathcal{H}_\alpha)$. Then, for sufficiently large N, determined by the requirements of the application at hand, the probability (42) can be well approximated by

$$\hat{\mathsf{P}}(\underline{t} \in \mathcal{P}_i^\iota | \mathcal{H}_\alpha) = \frac{\sum_{s=1}^{N} p_i^\iota(t^{(s)})}{N}, \text{ for } \iota = \text{I}, \ldots, \text{IV} \tag{43}$$

The difference between the four DIA-estimators in terms of the probability (41) is driven by the difference in their corresponding partitioning regions through $\mathsf{P}(\underline{t} \in \mathcal{P}_i^\iota | \mathcal{H}_\alpha)$. If the individual probabilities $\mathsf{P}[\chi^2(n, \lambda_{i\alpha}) \le \tau^2]$ all take the same value, then, since $\sum_{i=0}^{k} \mathsf{P}^\iota(\underline{t} \in \mathcal{P}_i | \mathcal{H}_\alpha) = 1$ and $\sum_{\alpha=0}^{k} \mathsf{P}[\mathcal{H}_\alpha] = 1$, the probability (41) would become identical across all the four DIA-estimators. This comes close to reality when, e.g. $\tau \to 0$ or $\tau \to \infty$, and/or $A^+ C_\alpha b_\alpha \to 0$ for all $\alpha \in [1, \ldots, k]$ (small influential biases).

We note that $\mathsf{P}[\mathcal{H}_0]$ is usually much larger than $\mathsf{P}[\mathcal{H}_{\alpha\neq 0}]$. In the limit when $\mathsf{P}[\mathcal{H}_0] \to 1$, the maximization problem in (38) reduces to

$$i = \arg \max_{j\in[0,\ldots,k]} \mathsf{P}[\underline{\chi}^2(n, \lambda_{j0}) \le \tau^2] \tag{44}$$

The solution to this problem is $i = 0$, implying that one would always accept the null hypothesis, i.e. $\mathcal{P}_0^{\text{III}} \to \mathbb{R}^r$. This is also the case with the testing procedure in (30), i.e. $\mathcal{P}_0^{\text{II}} \to \mathbb{R}^r$, as $S_{j\neq 0}^{\text{II}} \to \infty$ when $\mathsf{P}[\mathcal{H}_0] \to 1$. Therefore, the DIA-estimators $\underline{\bar{x}}^{\text{II}}$ and $\underline{\bar{x}}^{\text{III}}$ would have similar probabilistic properties, and thus similar values for (41), when $\mathsf{P}[\mathcal{H}_0] \to 1$, as both would approach $\underline{\hat{x}}_0$. Note that if $\mathcal{P}_0$ is constrained, then in (44), $[0, \ldots, k]$ is replaced with $[1, \ldots, k]$. This results in selecting the index of the alternative hypothesis with the smallest noncentrality parameter λ_{j0}, which, for the current simple example, corresponds to the alternative with the smallest bias magnitude. For example, if b_1 has the smallest magnitude among the biases, then $\mathcal{H}_1$ would always be accepted if the null hypothesis is rejected, i.e. $\mathcal{P}_1^{\text{IV}} \to \mathbb{R}^r \setminus \mathcal{P}_0^{\text{IV}}$. Consequently, the DIA estimator $\underline{\bar{x}}^{\text{IV}}$ would be driven solely by $\underline{\hat{x}}_0$ and $\underline{\hat{x}}_1$, with their contribution determined by P_{FA}.

In Fig. 5, the panels in the first row show $\mathsf{P}(\underline{\bar{x}}^{\mathrm{III}} \in \Omega_x)$ as a function of τ^2 (cf. 35) for $\mathsf{P}[\mathcal{H}_0] = 0.9,\ 0.99$, assuming different ranges of bias values $b = [b_1,\ b_2,\ b_3]$. The panels from the second row downward show the differences between $\mathsf{P}(\underline{\bar{x}}^{\mathrm{III}} \in \Omega_x)$ and each of the probabilities $\mathsf{P}(\underline{\bar{x}}^{\mathrm{IV}} \in \Omega_x)$, $\mathsf{P}(\underline{\bar{x}}^{\mathrm{II}} \in \Omega_x)$ and $\mathsf{P}(\underline{\bar{x}}^{\mathrm{I}} \in \Omega_x)$, respectively. These probabilities have been computed numerically using (43) with $N = 10^6$. The probability $\mathsf{P}(\underline{\bar{x}}^{\mathrm{III}} \in \Omega_x)$ shows only marginal sensitivity to changes in the values of the biases and $\mathsf{P}[\mathcal{H}_0]$. As expected, all the graphs from the second row onward in Fig. 5 take values close to zero when $\tau^2 \to 0$, and they approach zero again as $\tau^2 \to \infty$.

The probability $\mathsf{P}(\underline{\bar{x}}^{\mathrm{II}} \in \Omega_x)$ closely follows $\mathsf{P}(\underline{\bar{x}}^{\mathrm{III}} \in \Omega_x)$ particularly when $\mathsf{P}[\mathcal{H}_0]$ is close to one. It is observed that as the biases and their differences become larger, the difference between these two probabilities take on smaller values. This is consistent with Figs. 2 [right] and 3 [right], which show that the partitioning regions $\mathcal{P}^{\mathrm{II}}_{i\in[0,\ldots,3]}$ and $\mathcal{P}^{\mathrm{III}}_{i\in[0,\ldots,3]}$ converge as the biases become larger. We also note that the small probability difference between $\mathsf{P}(\underline{\bar{x}}^{\mathrm{III}} \in \Omega_x)$ and $\mathsf{P}(\underline{\bar{x}}^{\mathrm{II}} \in \Omega_x)$ for $b = [5,\ 10,\ 20]$ exhibits significant variability across simulation runs. This variability can be mitigated by using a larger number of samples, N, or by applying variance-reduction techniques, see, e.g. (Kroese et al. 2011). Furthermore, the difference between $\mathsf{P}(\underline{\bar{x}}^{\mathrm{III}} \in \Omega_x)$ and $\mathsf{P}(\underline{\bar{x}}^{\mathrm{II}} \in \Omega_x)$ can take large values depending on the influence of biases on the estimator $\underline{\hat{x}}_0$, referred to as *influential biases*. As (37) shows, the penalty functions (36) are driven by these influential, i.e. non-testable, biases $P_A c_i b_i$ $(i = 1, \ldots, k)$, where $P_A = AA^+$ represents the projector that orthogonally projects, in the metric of Q_{yy}, onto the range space of matrix A (Teunissen 2024a). The partitioning $\mathcal{P}^{\mathrm{III}}_{i\in[0,\ldots,k]}$, through its choice of penalty functions, seeks to mitigate the influence of these influential biases, which is not the case with the partitioning $\mathcal{P}^{\mathrm{II}}_{i\in[0,\ldots,k]}$ which uses a set of fixed penalty functions, i.e. $\{0, 1\}$. For the current example, the c_i vectors form an angle of approximately 55° with the range space of A, suggesting that almost 50% of the observation bias $c_i b_i$ is testable, while the remaining 50% is influential. Now, consider a new set of fault lines

$$c_1 = \begin{bmatrix} 1 \\ 1 \\ 0.99 \end{bmatrix},\ c_2 = \begin{bmatrix} 1 \\ 0.99 \\ 1 \end{bmatrix},\ c_3 = \begin{bmatrix} 0.99 \\ 1 \\ 1 \end{bmatrix} \tag{45}$$

which are almost aligned with the range space of A. The observation biases happening along the above fault lines are almost non-testable as $c_{t_i} \approx 0$. The difference between $\mathsf{P}(\underline{\bar{x}}^{\mathrm{III}} \in \Omega_x)$ and $\mathsf{P}(\underline{\bar{x}}^{\mathrm{II}} \in \Omega_x)$ for this case, assuming $b_1 = 1,\ b_2 = 2,\ b_3 = 4$, is illustrated in Fig. 6. As shown, this difference can now take large values.

The probabilities $\mathsf{P}(\underline{\bar{x}}^{\mathrm{IV}} \in \Omega_x)$ and $\mathsf{P}(\underline{\bar{x}}^{\mathrm{I}} \in \Omega_x)$ in Fig. 5 show significant differences from $\mathsf{P}(\underline{\bar{x}}^{\mathrm{III}} \in \Omega_x)$. The magnitude of these differences increases as the biases and their differences grow, P_{FA} becomes larger, and/or $\mathsf{P}[\mathcal{H}_0]$ approaches one. When $\mathsf{P}[\mathcal{H}_0]$ is sufficiently close to one, $\underline{\bar{x}}^{\mathrm{III}}$ can be approximated by $\underline{\hat{x}}_0$, leading to the following approximation

$$\mathsf{P}(\underline{\bar{x}}^{\mathrm{III}} \in \Omega_x) - \mathsf{P}(\underline{\bar{x}}^{\iota} \in \Omega_x) \approx \sum_{\substack{i=1 \\ \iota = \mathrm{I},\ \mathrm{IV}}}^{k} [\mathsf{P}(\underline{\hat{x}}_0 \in \Omega_x | \mathcal{H}_0) - \mathsf{P}(\underline{\hat{x}}_i \in \Omega_x | \mathcal{H}_0)] \mathsf{P}(\underline{t} \in \mathcal{P}^{\iota}_i | \mathcal{H}_0), \tag{46}$$

with $\sum_{i=1}^{k} \mathsf{P}(\underline{t} \in \mathcal{P}^{\iota}_i | \mathcal{H}_0) = \mathsf{P}_{\mathrm{FA}}$. Reducing P_{FA} by, for example, a factor of 10 results in a proportional decrease in the probability difference (46), which is corroborated by the second and fourth rows in Fig. 5. When the biases grow, while $\mathsf{P}(\underline{\hat{x}}_0 \in \Omega_x | \mathcal{H}_0)$ remain invariant, $\mathsf{P}(\underline{\hat{x}}_i \in \Omega_x | \mathcal{H}_0)$ becomes smaller, leading to larger values for $[\mathsf{P}(\underline{\hat{x}}_0 \in \Omega_x | \mathcal{H}_0) - \mathsf{P}(\underline{\hat{x}}_i \in \Omega_x | \mathcal{H}_0)]$. In the extreme case, when for example $b_i << b_j$ for all $j \neq i$, then, as also confirmed by Figs. 1 and 3, $\mathcal{P}^{\iota}_i$ grows at the cost of shrinking $\mathcal{P}^{\iota}_{j\neq i}$. Consequently, $\mathsf{P}(\underline{t} \in \mathcal{P}^{\iota}_i | \mathcal{H}_0) \to \mathsf{P}_{\mathrm{FA}}$ while $\mathsf{P}(\underline{t} \in \mathcal{P}^{\iota}_{j\neq i} | \mathcal{H}_0) \to 0$. In this case, (46) can be approximated by $[\mathsf{P}(\underline{\hat{x}}_0 \in \Omega_x | \mathcal{H}_0) - \mathsf{P}(\underline{\hat{x}}_i \in \Omega_x | \mathcal{H}_0)] \mathsf{P}_{\mathrm{FA}}$ which is an increasing function of b_i.

As the user controls the false alarm probability when $\mathcal{P}_0$ is set by the OMT, it may motivate a comparison of the DIA estimators $\underline{\bar{x}}^{\mathrm{I}}$ and $\underline{\bar{x}}^{\mathrm{IV}}$ against $\underline{\bar{x}}^{\mathrm{III}}$ for the same probability of false alarms. This probability for the partitioning $\mathcal{P}^{\mathrm{III}}_{i\in[0,\ldots,k]}$ can be numerically computed using the approximation in (43). Note that, in addition to the bias values, P_{FA} for $\mathcal{P}^{\mathrm{III}}_{i\in[0,\ldots,k]}$ also depends on τ^2. Figure 7 illustrates the probability differences $\mathsf{P}(\underline{\bar{x}}^{\mathrm{III}} \in \Omega_x) - \mathsf{P}(\underline{\bar{x}}^{\mathrm{IV}} \in \Omega_x)$ (solid lines) and $\mathsf{P}(\underline{\bar{x}}^{\mathrm{III}} \in \Omega_x) - \mathsf{P}(\underline{\bar{x}}^{\mathrm{I}} \in \Omega_x)$ (bold lines), along with P_{FA} associated with $\mathcal{P}^{\mathrm{III}}_{i\in[0,\ldots,k]}$ (dashed lines) as a function of τ^2 for different sets of biases, assuming $\mathsf{P}[\mathcal{H}_0] = 0.9$.

All the probability differences in Fig. 5 initially show an increasing trend as a function of τ^2, followed by a decrease, and eventually stabilize. We explain this behavior for the bottom panels, making the simplifying assumption that $\mathsf{P}[\mathcal{H}_0]$ is sufficiently close to one, such that the approximation (46) can be used. As Ω_x is an x-centered region and the PDF of $\underline{\hat{x}}_0$ is more peaked around x than the PDF of $\underline{\hat{x}}_{i\neq 0}$, when τ^2 starts increasing from zero, $\mathsf{P}(\underline{\hat{x}}_0 \in \Omega_x | \mathcal{H}_0)$ increases more rapidly than $\mathsf{P}(\underline{\hat{x}}_{i\neq 0} \in \Omega_x | \mathcal{H}_0)$. This, along with the fact that these probabilities are continuous functions of τ^2 and that their difference approaches zero when $\tau^2 \to 0$ or $\tau^2 \to \infty$, results in an increasing and then decreasing behavior of the probability difference in (46).

4.2 Surveying example

To determine the three-dimensional coordinates of a point, denoted by $[\mathsf{e}, \mathsf{n}, \mathsf{h}]^T \in \mathbb{R}^3$, five distance measurements are

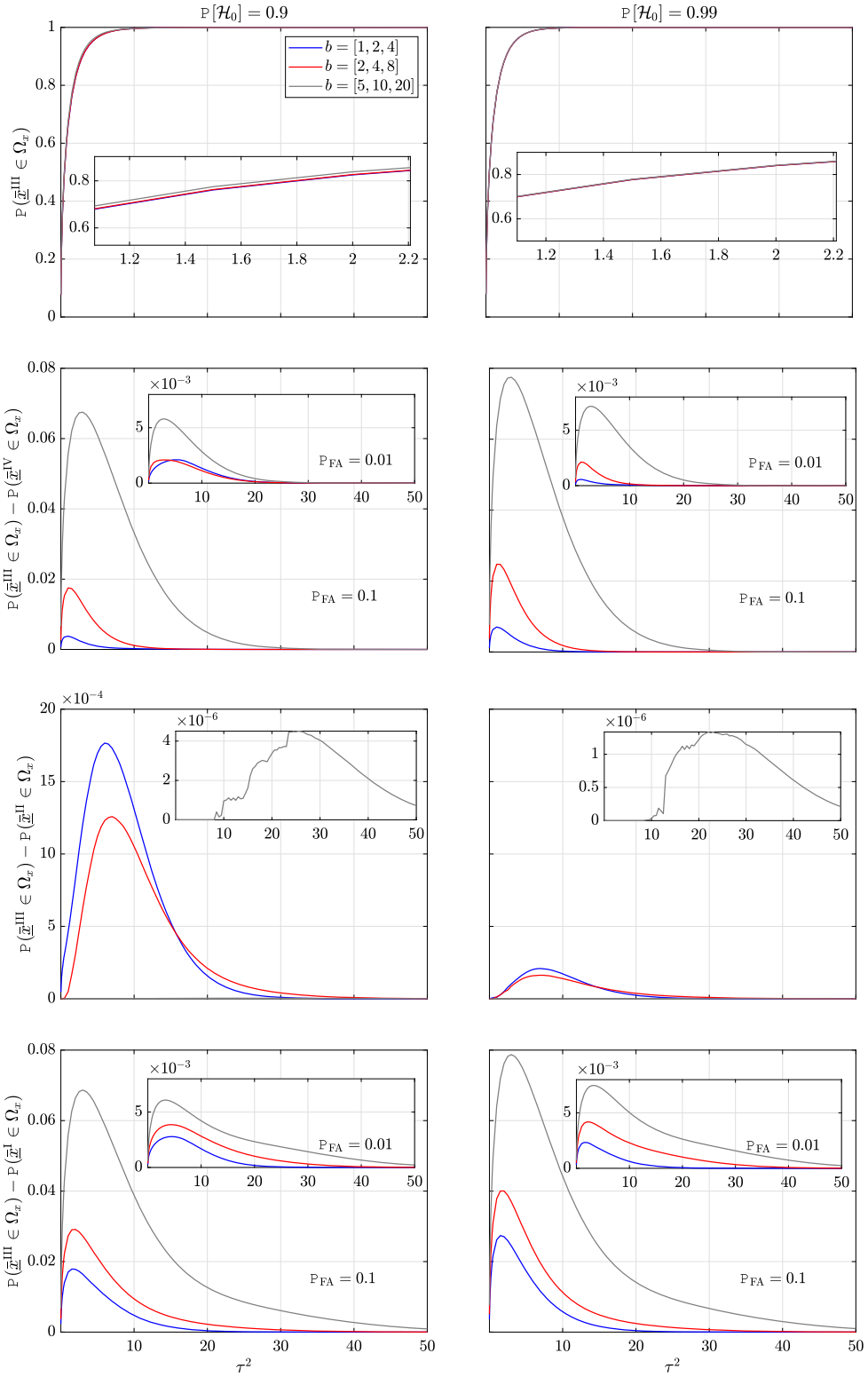

Fig. 5 Comparison of the DIA-estimators $\underline{\bar{x}}^{\iota}$ for $\iota \in \{\mathrm{I}, \ldots, \mathrm{IV}\}$ corresponding with the simple example. These results are obtained assuming $\mathsf{P}[\mathcal{H}_{i\neq 0}] = (1 - \mathsf{P}[\mathcal{H}_0])/3$. [First row] The probability $\mathsf{P}(\underline{\bar{x}}^{\mathrm{III}} \in \Omega_x)$ as a function of τ^2, with a zoom-in view. [Second row] The difference between $\mathsf{P}(\underline{\bar{x}}^{\mathrm{III}} \in \Omega_x)$ and $\mathsf{P}(\underline{\bar{x}}^{\mathrm{IV}} \in \Omega_x)$ as a function of τ^2 for $\mathsf{P}_{\mathrm{FA}} = 0.1$ with an inset panel showing the result for $\mathsf{P}_{\mathrm{FA}} = 0.01$. [Third row] The difference between $\mathsf{P}(\underline{\bar{x}}^{\mathrm{III}} \in \Omega_x)$ and $\mathsf{P}(\underline{\bar{x}}^{\mathrm{II}} \in \Omega_x)$ as a function of τ^2, with a zoom-in view. [Fourth row] The difference between $\mathsf{P}(\underline{\bar{x}}^{\mathrm{III}} \in \Omega_x)$ and $\mathsf{P}(\underline{\bar{x}}^{\mathrm{I}} \in \Omega_x)$ as a function of τ^2 for $\mathsf{P}_{\mathrm{FA}} = 0.1$ with an inset panel showing the result for $\mathsf{P}_{\mathrm{FA}} = 0.01$. [Left] $\mathsf{P}(\mathcal{H}_0) = 0.9$. [Right] $\mathsf{P}(\mathcal{H}_0) = 0.99$

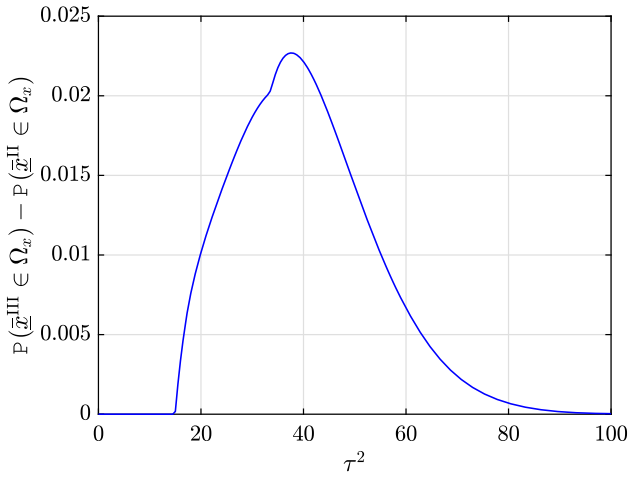

Fig. 6 The difference between $\mathsf{P}(\underline{\bar{x}}^{\mathrm{III}} \in \Omega_x)$ and $\mathsf{P}(\underline{\bar{x}}^{\mathrm{II}} \in \Omega_x)$ as a function of τ^2 for (45), assuming $b_1 = 1,\ b_2 = 2,\ b_3 = 4$, $\mathsf{P}(\mathcal{H}_0) = 0.9$, and $\mathsf{P}[\mathcal{H}_{i\neq 0}] = (1 - \mathsf{P}[\mathcal{H}_0])/3$

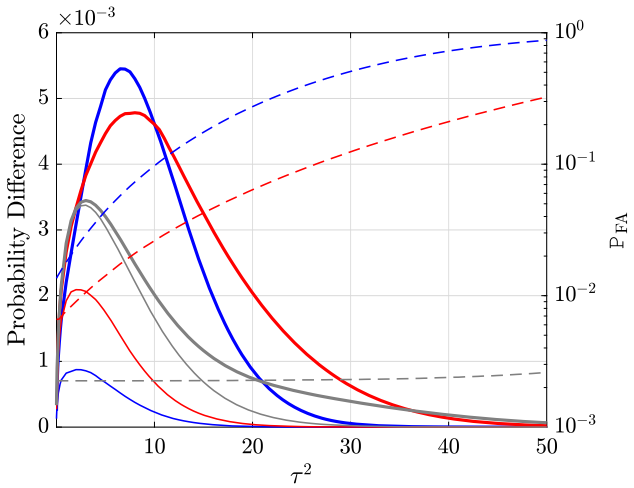

Fig. 7 [Left axis] The probability differences $\mathsf{P}(\underline{\bar{x}}^{\mathrm{III}} \in \Omega_x) - \mathsf{P}(\underline{\bar{x}}^{\mathrm{IV}} \in \Omega_x)$ (solid lines) and $\mathsf{P}(\underline{\bar{x}}^{\mathrm{III}} \in \Omega_x) - \mathsf{P}(\underline{\bar{x}}^{\mathrm{I}} \in \Omega_x)$ (bold lines) as a function of τ^2. [Right axis] P_{FA} associated with $\mathcal{P}^{\mathrm{III}}_{i\in[0,\ldots,k]}$ (dashed lines) as a function of τ^2. The results are presented for different sets of biases: $b = [1, 2, 4]$ (blue), $b = [2, 4, 8]$ (red) and $b = [5, 10, 20]$ (gray), assuming $\mathsf{P}[\mathcal{H}_0] = 0.9$ and $\mathsf{P}[\mathcal{H}_{i\neq 0}] = (1 - \mathsf{P}[\mathcal{H}_0])/3$

designed between the point and five different Permanent Survey Marks (PSMs), i.e. PSM_i for $i = 1, \ldots, 5$, with known coordinates $[\mathsf{e}_i, \mathsf{n}_i, \mathsf{h}_i]^T$ as shown in Fig. 8. We assume that the unknown point is occupied by a total station taking slope distance measurements to the prism reflectors set up on the PSMs. Under the null hypothesis $\mathcal{H}_0$, it is assumed that all of the five prisms are of the same type, say 'Type-1', with a known prism constant. Under $\mathcal{H}_0$, the linearized observation equation of the slope distance measured from the unknown point to PSM_i, reads

$$\mathcal{H}_0 : \ \mathsf{E}(\underline{d}_i) = u_i^T x, \qquad i = 1, \ldots, 5 \tag{47}$$

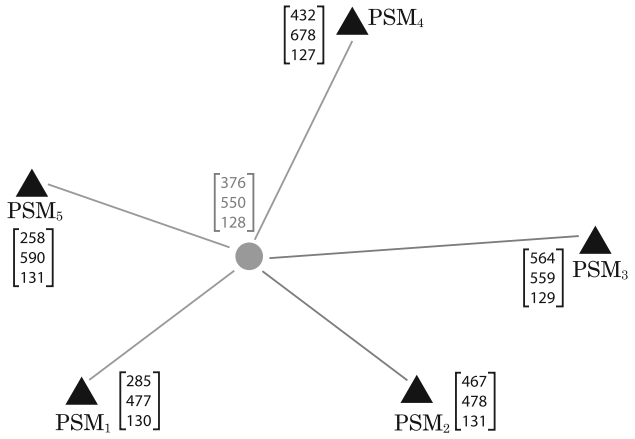

Fig. 8 A geodetic network, consisting of five PSMs (triangles) and one unknown point (circle). Using a total station over the unknown point, a slope distance is measured to the prism on each PSM. The known coordinates of each PSM and the approximate coordinates of the unknown point are shown next to them

with $\underline{d}_i$ the observed-minus-computed distance measurement corrected for the prism constant, $u_i = \frac{1}{l_i}[\mathsf{e} - \mathsf{e}_i,\ \mathsf{n} - \mathsf{n}_i,\ \mathsf{h} - \mathsf{h}_i + (\mathsf{h}_T - \mathsf{h}_{P_i})]^T$ the unit direction vector of the line of sight from prism to total station telescope, h_{P_i} the height of prism, h_T the height of total station, l_i the computed length of the line of sight and x the coordinate increment vector of the unknown point. Note, in the following, that we assume $\mathsf{h}_T = \mathsf{h}_{P_1} = \ldots = \mathsf{h}_{P_5}$.

The distance measurement errors are assumed to be uncorrelated and normally distributed, and also of the same standard deviation equal to $\sigma = 5$mm. The matrix–vector representation of (47) reads

$$\mathcal{H}_0 : \ \mathsf{E}(\underline{d}) = A\,x, \quad \mathsf{D}(\underline{d}) = \sigma^2 I_5 \tag{48}$$

with $\underline{d} = [\underline{d}_1, \ldots, \underline{d}_5]^T \in \mathbb{R}^5$ and $A = [u_1, \ldots, u_5]^T \in \mathbb{R}^{5\times 3}$. With $m = 5$ distance measurements and $n = 3$ unknown coordinate increments, the redundancy under $\mathcal{H}_0$ is $r = 2$. Now let us assume that there is a suspicion that one of the prisms is of another type, say 'Type-2', again with a known prism constant but differing from that of 'Type-1' by an amount of μ. In this case, five hypotheses alternative to (48) can be formed as

$$\mathcal{H}_i : \ \mathsf{E}(\underline{d}) = A\,x + c_i\mu, \quad \mathsf{D}(\underline{d}) = \sigma^2 I_5, \ i = 1, \ldots, 5 \tag{49}$$

Note that the biases under all the alternative hypotheses are of the same value, i.e. $b_i = \mu$ $(i = 1, \ldots, 5)$.

Assuming $\mu = 40$mm, $\mathsf{P}[\mathcal{H}_0] = 0.9$, $\mathsf{P}[\mathcal{H}_{i\neq 0}] = (1 - \mathsf{P}[\mathcal{H}_0])/5$ and $\mathsf{P}_{\mathrm{FA}} = 0.001$, Fig. 9, from left to right, illustrates the partitionings (21)+(25), (30), (38) and its $\mathcal{P}_0$-constrained variant with $\tau^2 = 60$. Note that the misclosure

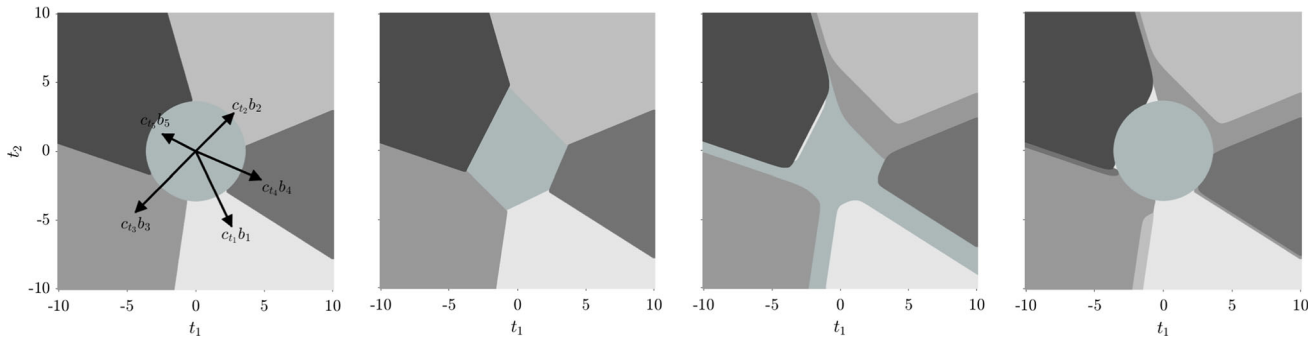

Fig. 9 Misclosure space partitioning corresponding with the surveying example. The panels, from left to right, show $\mathcal{P}^{\iota}_{i\in[0,\ldots,5]}$, for $\iota \in \{\mathrm{I},\ldots,\mathrm{IV}\}$, respectively, whereby the partitioning regions are displayed in different shades of gray, getting darker as i increases from 1 to 5, with $\mathcal{P}^{\iota}_0$ shown in green. These results are obtained assuming $\mu = 40$mm, $\mathsf{P}[\mathcal{H}_0] = 0.9$, $\mathsf{P}[\mathcal{H}_{i\neq 0}] = (1-\mathsf{P}[\mathcal{H}_0])/5$, $\mathsf{P}_{\mathrm{FA}} = 0.001$ and $\tau^2 = 60$

is formed by

$$B = \begin{bmatrix} 66.092 & -137.603 \\ 70.339 & 70.181 \\ -110.96 & -111.547 \\ 120.377 & -51.793 \\ -62.302 & 31.855 \end{bmatrix} \tag{50}$$

whose elements are shown to three decimal places, and yields $Q_{tt} = I_2$. The partitioning regions $\mathcal{P}^{\iota}_{i\in[1,\ldots,5]}$, for $\iota \in \{\mathrm{I},\ldots,\mathrm{IV}\}$, are shown in different shades of gray, getting darker as i increases from 1 to 5, with $\mathcal{P}^{\iota}_0$ shown in green. In addition, $\mathsf{E}(\underline{t}|\mathcal{H}_i) = c_{t_i} b_i$ for $i = 1,\ldots,5$ are also shown as black vectors in the left panel. The relative orientation of these vectors is determined by the geometry of the network. For instance, the angle between two vectors c_{t_i} and c_{t_j} can be computed from (Zaminpardaz and Teunissen 2019)

$$\cos\angle(c_{t_i}, c_{t_j}) = \frac{-\bar{u}_i^T \bar{u}_j}{\sqrt{\left(1-\|\bar{u}_i\|^2\right)\times\left(1-\|\bar{u}_j\|^2\right)}} \tag{51}$$

where $\bar{u}_i = \mathcal{G}^{-T} u_i$ with $\mathcal{G}^T$ the Cholesky-factor of the Cholesky-factorization $C_{xx} = \sum_{l=1}^{m} u_l u_l^T = \mathcal{G}^T\mathcal{G}$. The above equation results from the identity $B\,Q_{tt}^{-1}B^T = Q_{yy}^{-1} - Q_{yy}^{-1}A\,Q_{\hat{x}_0\hat{x}_0}A^T\,Q_{yy}^{-1}$ with $Q_{\hat{x}_0\hat{x}_0} = \sigma^2 C_{xx}^{-1}$, and also the fact that the B matrix in use corresponds to $Q_{tt} = I_2$. Therefore the angle between c_{t_i} and c_{t_j} is determined by the angle between $\bar{u}_i$ and $\bar{u}_j$ as well as their length. For the network geometry illustrated in Fig. 8, we have

$$\bar{u}_1 = \begin{bmatrix} 0.431 \\ 0.457 \\ -0.152 \end{bmatrix},\ \bar{u}_2 = \begin{bmatrix} -0.433 \\ 0.494 \\ -0.567 \end{bmatrix},\ \bar{u}_3 = \begin{bmatrix} -0.552 \\ -0.010 \\ -0.277 \end{bmatrix},$$
$$\bar{u}_4 = \begin{bmatrix} -0.221 \\ -0.689 \\ -0.218 \end{bmatrix},\ \bar{u}_5 = \begin{bmatrix} 0.523 \\ -0.270 \\ -0.729 \end{bmatrix} \tag{52}$$

These values, rounded to three decimal places, in tandem with (51) explain why c_{t_2} and c_{t_3} are almost parallel, as well as why c_{t_4} and c_{t_5} are almost parallel.

As shown in Fig. 9, due to the assumption that $\mathsf{P}[\mathcal{H}_i] = \mathsf{P}[\mathcal{H}_j]$ for $i \neq j$, the boundaries separating the regions $\mathcal{P}^{\mathrm{II}}_{i\neq 0}$ and $\mathcal{P}^{\mathrm{II}}_{j\neq 0}$, as well as those separating $\mathcal{P}^{\mathrm{I}}_{i\neq 0}$ and $\mathcal{P}^{\mathrm{I}}_{j\neq 0}$ for $i, j = 1,\ldots,5$, are situated on the same hyperplanes. Comparing the two middle panels, we note that changing the penalties from $\{0, 1\}$ to $\mathsf{P}[\underline{\chi}^2(n,\lambda_{j\alpha}) > \tau^2]$ causes the $\mathcal{H}_0$ region leak between those of $\mathcal{H}_1$-$\mathcal{H}_3$, $\mathcal{H}_1$-$\mathcal{H}_4$, and $\mathcal{H}_3$-$\mathcal{H}_5$. In addition, the $\mathcal{H}_3$ region leak between those of $\mathcal{H}_0$-$\mathcal{H}_2$ and $\mathcal{H}_2$-$\mathcal{H}_4$. This behavior can be understood by examining the penalty matrix corresponding to $\mathcal{P}^{\mathrm{III}}_{i\in[0,\ldots,5]}$, which, to three decimal places, is given by

$$\begin{bmatrix} 0.000 & 0.008 & 0.253 & 0.004 & 0.060 & 0.452 \\ 0.008 & 0.000 & 0.523 & 0.872 & 0.998 & 0.439 \\ 0.253 & 0.523 & 0.000 & 0.002 & 0.991 & 0.988 \\ 0.004 & 0.872 & 0.002 & 0.000 & 0.061 & 0.973 \\ 0.060 & 0.998 & 0.991 & 0.061 & 0.000 & 0.635 \\ 0.452 & 0.439 & 0.988 & 0.973 & 0.635 & 0.000 \end{bmatrix} \tag{53}$$

The entries of the matrix are determined by the geometry of the network shown in Fig. 8, through the relationship

$$\lambda_{j\alpha} = \frac{\mu^2}{\sigma^2}\|\bar{u}_j - \bar{u}_\alpha\|^2 \tag{54}$$

with $\bar{u}_0 = 0$. The penalty for selecting $\mathcal{H}_j$ under $\mathcal{H}_\alpha$ (and vice versa) increases with the distance between the vectors $\bar{u}_j$ and $\bar{u}_\alpha$, and decreases as the distance becomes smaller.

From (53), it can be seen that the penalties associated with the pairs $\mathcal{H}_1$-$\mathcal{H}_3$ and $\mathcal{H}_1$-$\mathcal{H}_4$ are over 100 times greater than that of the pair $\mathcal{H}_0$-$\mathcal{H}_1$. This explains why $\mathcal{P}^{\mathrm{III}}_1$ is fully encompassed by $\mathcal{P}^{\mathrm{III}}_0$, and shares no common borders with $\mathcal{P}^{\mathrm{III}}_3$ or $\mathcal{P}^{\mathrm{III}}_4$. Similarly, the penalty for the pair $\mathcal{H}_3$-$\mathcal{H}_5$ exceeds that of $\mathcal{H}_0$-$\mathcal{H}_3$ by more than 240 times, resulting in no shared

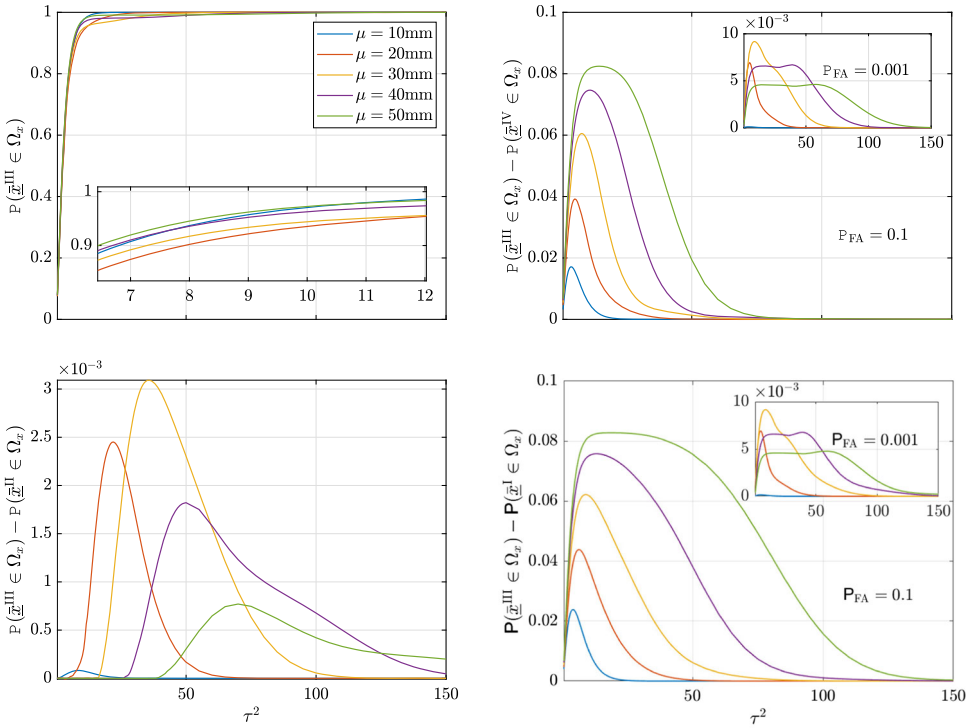

Fig. 10 Comparison of the DIA-estimators $\underline{\bar{x}}^{\iota}$ for $\iota \in \{\mathrm{I}, \ldots, \mathrm{IV}\}$ corresponding with Fig. 8. These results are obtained assuming $\mathrm{P}[\mathcal{H}_0] = 0.9$ and $\mathrm{P}[\mathcal{H}_{i\neq 0}] = (1 - \mathrm{P}[\mathcal{H}_0])/5$. [Top-left] The probability $\mathrm{P}(\underline{\bar{x}}^{\mathrm{III}} \in \Omega_x)$ as a function of τ^2, with a zoom-in view. [Top-right] The difference between $\mathrm{P}(\underline{\bar{x}}^{\mathrm{III}} \in \Omega_x)$ and $\mathrm{P}(\underline{\bar{x}}^{\mathrm{IV}} \in \Omega_x)$ as a function of τ^2 for $\mathrm{P}_{\mathrm{FA}} = 0.1$ with an inset panel showing the result for $\mathrm{P}_{\mathrm{FA}} = 0.001$. [Bottom-left] The difference between $\mathrm{P}(\underline{\bar{x}}^{\mathrm{III}} \in \Omega_x)$ and $\mathrm{P}(\underline{\bar{x}}^{\mathrm{II}} \in \Omega_x)$ as a function of τ^2. [Bottom-right] The difference between $\mathrm{P}(\underline{\bar{x}}^{\mathrm{III}} \in \Omega_x)$ and $\mathrm{P}(\underline{\bar{x}}^{\mathrm{I}} \in \Omega_x)$ as a function of τ^2 for $\mathrm{P}_{\mathrm{FA}} = 0.1$ with an inset panel showing the result for $\mathrm{P}_{\mathrm{FA}} = 0.001$

border between $\mathcal{P}_3^{\mathrm{III}}$ and $\mathcal{P}_5^{\mathrm{III}}$. In contrast to the second panel (from the left), the region corresponding to $\mathcal{H}_2$ in the third panel does not share borders with $\mathcal{H}_0$, $\mathcal{H}_4$ and $\mathcal{H}_5$, but instead shares a border with $\mathcal{H}_3$. This is due to the penalties for the pairs $\mathcal{H}_0$-$\mathcal{H}_2$, $\mathcal{H}_2$-$\mathcal{H}_4$ and $\mathcal{H}_2$-$\mathcal{H}_5$ being larger than that of $\mathcal{H}_2$-$\mathcal{H}_3$ by factors of 127, 496 and 494, respectively.

Comparing the two panels on the right of Fig. 9, we observe that constraining $\mathcal{P}_0$ to be determined by the overall model test does not result in significant changes to the geometry of the regions corresponding to $\mathcal{H}_{\alpha\in[1,\ldots,k]}$. The primary difference is that the $\mathcal{H}_0$ region, located between these regions in the second panel (from the right), is replaced by regions of the alternative hypotheses, depending on the corresponding penalties. For instance, the region of $\mathcal{H}_4$ extends between $\mathcal{H}_3$ and $\mathcal{H}_5$ as the penalty for the pair $\mathcal{H}_3$-$\mathcal{H}_4$ is 16 times smaller than that for $\mathcal{H}_3$-$\mathcal{H}_5$.

A comparison among the four DIA-estimators $\underline{\bar{x}}^{\iota}$ for $\iota = \mathrm{I}, \ldots, \mathrm{IV}$ is shown in Fig. 10, assuming $\mathrm{P}[\mathcal{H}_0] = 0.9$, $\mathrm{P}[\mathcal{H}_{i\neq 0}] = (1 - \mathrm{P}[\mathcal{H}_0])/5$, $\mu = 10, 20, 30, 40, 50$mm and $\mathrm{P}_{\mathrm{FA}} = 0.1,\ 0.001$. Similar to our observations from Fig. 5, there can be significant differences between $\mathrm{P}(\underline{\bar{x}}^{\mathrm{I}} \in \Omega_x)$ and $\mathrm{P}(\underline{\bar{x}}^{\mathrm{III}} \in \Omega_x)$, as well as between $\mathrm{P}(\underline{\bar{x}}^{\mathrm{IV}} \in \Omega_x)$ and $\mathrm{P}(\underline{\bar{x}}^{\mathrm{III}} \in \Omega_x)$ depending on μ, τ^2, and P_{FA}. While $\mathrm{P}(\underline{\bar{x}}^{\mathrm{II}} \in \Omega_x)$ closely follows $\mathrm{P}(\underline{\bar{x}}^{\mathrm{III}} \in \Omega_x)$ for the considered alternative hypotheses, their difference can become significant if these hypotheses are replaced by ones describing more influential observation biases, as seen in the simple model. For instance, in (49), angles of approximately 50° are formed by c_1 and c_3 with the range space of A. By substituting them

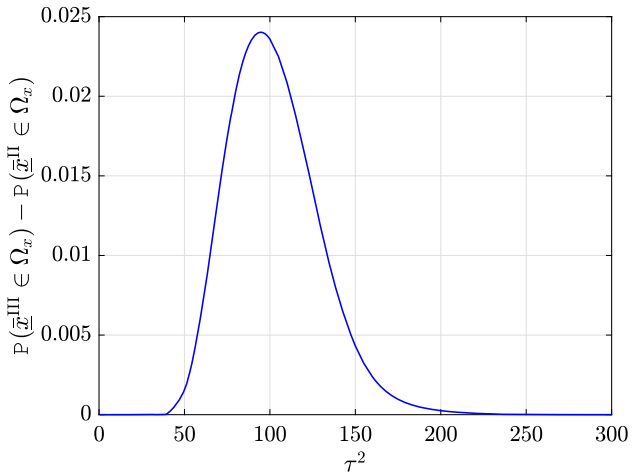

Fig. 11 The difference between $\mathrm{P}(\underline{\bar{x}}^{\mathrm{III}} \in \Omega_x)$ and $\mathrm{P}(\underline{\bar{x}}^{\mathrm{II}} \in \Omega_x)$ as a function of τ^2 for (55), assuming $\mu = 40$mm, $\mathrm{P}(\mathcal{H}_0) = 0.9$, and $\mathrm{P}[\mathcal{H}_{i\neq 0}] = (1 - \mathrm{P}[\mathcal{H}_0])/5$.

with the following fault lines

$$c_1 = \begin{bmatrix} 0 \\ 1 \\ 1 \\ 0 \\ 0 \end{bmatrix}, \quad c_3 = \begin{bmatrix} 0 \\ 0 \\ 0 \\ 1 \\ 1 \end{bmatrix} \tag{55}$$

which describe the use of Type-2 prisms on survey point pairs PSM_2-PSM_3 and PSM_4-PSM_5, respectively, these new fault lines form angles of around 12° with the range space

of A. Consequently, the observation biases along these new fault lines are much more influential compared to their counterparts in (49). The difference between $\mathsf{P}(\underline{\bar{x}}^{\mathrm{III}} \in \Omega_x)$ and $\mathsf{P}(\underline{\bar{x}}^{\mathrm{II}} \in \Omega_x)$ for this case, assuming $\mu = 40$mm, is illustrated in Fig. 11, showing significantly larger values compared to the purple graph in Fig. 10 [bottom-left].

4.3 Leveling example

To establish three new survey points (P_1, P_2, P_3), a leveling loop is performed that includes these points as well as three benchmarks (BM_1, BM_2, BM_3) with known heights as shown in Fig. 12. The loop, consisting of six instrument set-ups, starts and finishes at BM_1 progressing in a clockwise direction. Let $\underline{\Delta h} \in \mathbb{R}^6$ contain the measured height differences between successive points. We define $\underline{y} = \underline{\Delta h} + [h_{\mathrm{BM}_1}, h_{\mathrm{BM}_2} e_2^{\perp T}, h_{\mathrm{BM}_3} e_2^{\perp T}, -h_{\mathrm{BM}_1}]^T$ with h_{BM_i} the known height of BM_i and $e_2^{\perp} = [-1,\ 1]^T$ being orthogonal to e_2. Under the null hypothesis, the observation equations to find the unknown heights of the survey points ($\mathrm{P}_1, \mathrm{P}_2, \mathrm{P}_3$), stacked in $x \in \mathbb{R}^3$, reads

$$\mathcal{H}_0 :\ \mathsf{E}(\underline{y}) = -(I_3 \otimes e_2^{\perp})\, x, \quad \mathsf{D}(\underline{y}) = \sigma^2 I_6 \tag{56}$$

with $\otimes$ the Kronecker product and σ the standard deviation of the height difference measurements which are assumed to be independent and equally precise. The redundancy under $\mathcal{H}_0$ is $r = 3$.

As Fig. 12 shows, BM_2' and BM_3' are in close proximity to BM_2 and BM_3, respectively. Therefore, it is suspected that BM_2 and/or BM_3 might have been confused with their nearby benchmarks. Let us assume that $h_{\mathrm{BM}_2'} - h_{\mathrm{BM}_2} = h_{\mathrm{BM}_3'} - h_{\mathrm{BM}_3} = \mu$ where μ is known. Then three hypotheses alternative to (56) can be defined as follows

$$\begin{aligned}
\mathcal{H}_1 :\ \mathsf{E}(\underline{y}) &= -(I_3 \otimes e_2^{\perp})\, x + \begin{bmatrix} 0 \\ -e_2^{\perp} \\ 0_3 \end{bmatrix} \mu,\ \mathsf{D}(\underline{y}) = \sigma^2 I_6 \\
\mathcal{H}_2 :\ \mathsf{E}(\underline{y}) &= -(I_3 \otimes e_2^{\perp})\, x + \begin{bmatrix} 0_3 \\ -e_2^{\perp} \\ 0 \end{bmatrix} \mu,\ \mathsf{D}(\underline{y}) = \sigma^2 I_6 \\
\mathcal{H}_3 :\ \mathsf{E}(\underline{y}) &= -(I_3 \otimes e_2^{\perp})\, x + \begin{bmatrix} 0 \\ -e_2^{\perp} \\ -e_2^{\perp} \\ 0 \end{bmatrix} \mu,\ \mathsf{D}(\underline{y}) = \sigma^2 I_6
\end{aligned} \tag{57}$$

Among the above alternatives, $\mathcal{H}_1$ describes the confusion of BM_2 with BM_2', $\mathcal{H}_2$ describes the confusion of BM_3 with BM_3', and $\mathcal{H}_3$ describes the confusion of both benchmarks with their nearby counterparts.

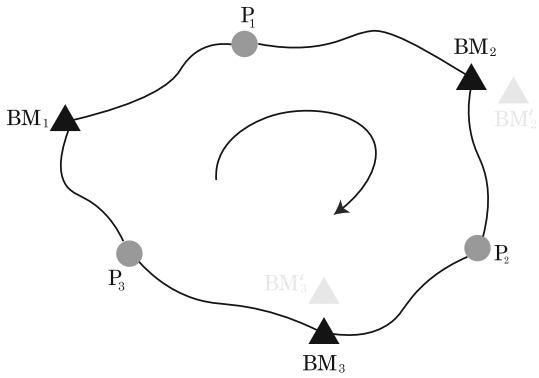

Fig. 12 A leveling network, consisting of a loop, running through six points with three of them being benchmarks (black triangles). The curved arrow in the middle indicates that the leveling progresses in a clockwise direction starting from and ending at BM_1. The curves between points indicate the observed height differences

Figure 13 shows a comparison among the four DIA-estimators $\underline{\bar{x}}^{\iota}$ for $\iota = \mathrm{I}, \ldots, \mathrm{IV}$, assuming $\sigma = 5$mm, $\mathsf{P}[\mathcal{H}_0] = 0.9$, $\mathsf{P}[\mathcal{H}_{i\neq 0}] = (1 - \mathsf{P}[\mathcal{H}_0])/3$, $\mathsf{P}_{\mathrm{FA}} = 0.1, 0.001$, and $\mu = 10, 20, 30$mm. We note that the graphs in the top right panel closely resemble those in the bottom right panel in terms of values. The results depicted in these figures are consistent with the trends identified in the previous examples.

5 Summary and conclusions

In this contribution, we studied four members from the class of DIA-estimators, whose misclosure-space partitionings are defined based on the concept of minimum mean penalty testing (Teunissen 2024a). This approach involves assigning penalty functions to each of the partitioning decision regions in misclosure space, calculating the mean penalty for each partitioning using the distribution of the misclosure vector, and identifying the partitioning that minimizes the mean penalty. Our focus was on cases where the biases under the alternative hypotheses were fully known.

The minimum-mean penalty partitionings we considered correspond to: I) the traditional DIA procedure, which combines the OMT with likelihood-ratio-based tests, and is commonly used in geodetic applications; II) maximizing probability of correct hypothesis identification; III) maximizing probability of correct parameter estimation; and IV) a $\mathcal{P}_0$-constrained version of III, where $\mathcal{P}_0$ was set to that of I. It was demonstrated that partitioning I is a special case of II when its $\mathcal{P}_0$ is determined by the OMT. We also discussed the conditions under which two hypotheses can be distinguished through the testing procedures associated with the mentioned partitionings.

To compare the four DIA-estimators, we examined their misclosure-space partitioning and evaluated the probabilities

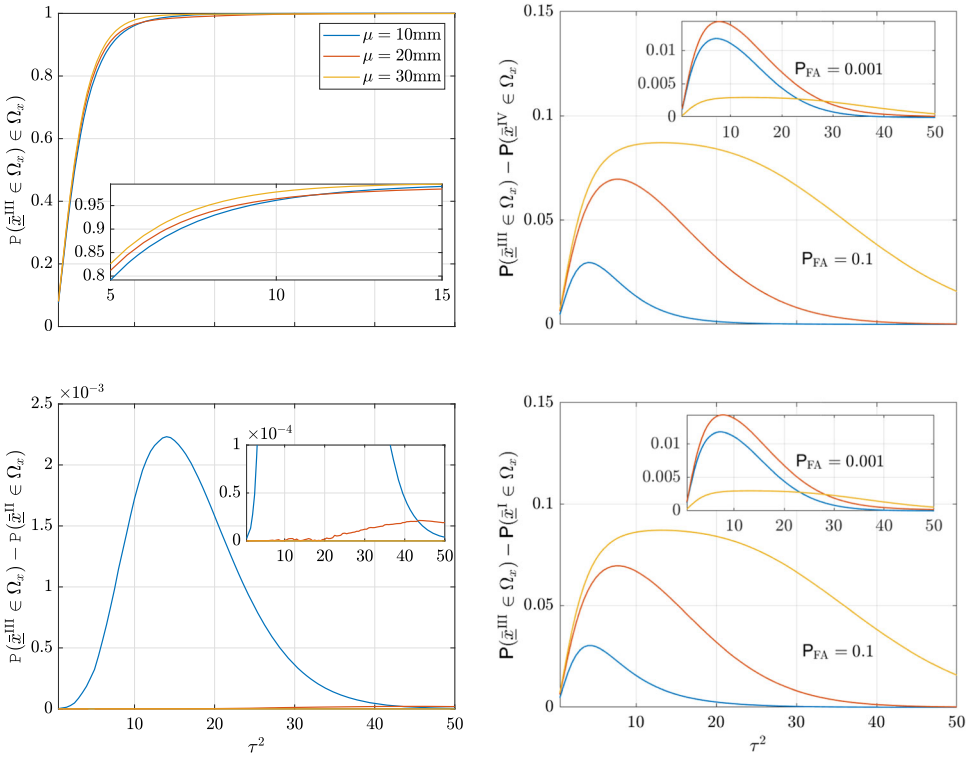

Fig. 13 Comparison of the DIA-estimators $\underline{\bar{x}}^{\iota}$ for $\iota \in \{\mathrm{I}, \ldots, \mathrm{IV}\}$ corresponding with Fig. 12. These results are obtained assuming $\mathrm{P}[\mathcal{H}_0] = 0.9$ and $\mathrm{P}[\mathcal{H}_{i\neq 0}] = (1 - \mathrm{P}[\mathcal{H}_0])/3$. [Top-left] The probability $\mathrm{P}(\underline{\bar{x}}^{\mathrm{III}} \in \Omega_x)$ as a function of τ^2, with a zoom-in view. [Top-right] The difference between $\mathrm{P}(\underline{\bar{x}}^{\mathrm{III}} \in \Omega_x)$ and $\mathrm{P}(\underline{\bar{x}}^{\mathrm{IV}} \in \Omega_x)$ as a function of τ^2 for $\mathrm{P}_{\mathrm{FA}} = 0.1$ with an inset panel showing the result for $\mathrm{P}_{\mathrm{FA}} = 0.001$. [Bottom-left] The difference between $\mathrm{P}(\underline{\bar{x}}^{\mathrm{III}} \in \Omega_x)$ and $\mathrm{P}(\underline{\bar{x}}^{\mathrm{II}} \in \Omega_x)$ as a function of τ^2, with a zoom-in view. [Bottom-right] The difference between $\mathrm{P}(\underline{\bar{x}}^{\mathrm{III}} \in \Omega_x)$ and $\mathrm{P}(\underline{\bar{x}}^{\mathrm{I}} \in \Omega_x)$ as a function of τ^2 for $\mathrm{P}_{\mathrm{FA}} = 0.1$ with an inset panel showing the result for $\mathrm{P}_{\mathrm{FA}} = 0.001$

of these estimators falling within an x-centered elliptical safety region. This analysis was conducted using three distinct examples: three repeat measurements of a single quantity, distance measurements in a three-dimensional geodetic network, and height-difference measurements in a leveling network. In all cases, we assumed that the alternative hypotheses were equally likely. It was discussed how the distinct penalty functions of III, compared to those of II, account for the differences in their partitionings. We observed that, depending on how influential the observation biases are, the DIA estimator of II can deviate significantly from III in terms of its probability of falling within the safety region. Additionally, significant differences can arise between the DIA estimators of I and IV relative to III. These differences depend on the size of the biases, the extent of the safety region, and the probability of false alarm.

Appendix

Proof of Lemma 1 'if' part: Let us assume that $\mathcal{P}^{\mathrm{I}}_{ij} = \mathcal{P}^{\mathrm{I}}_i \cap \mathcal{P}^{\mathrm{I}}_j \neq \emptyset$ for $i \neq j$. Then, for some $t \in \mathbb{R}^r \setminus \mathcal{P}^{\mathrm{I}}_0$, we have

$$\|t - C_{t_i} b_i\|^2_{Q_{tt}} = \|t - C_{t_j} b_j\|^2_{Q_{tt}} \tag{58}$$

or alternatively

$$2(C_{t_j} b_j - C_{t_i} b_i)^T Q_{tt}^{-1} t = \kappa_{ij} \tag{59}$$

with $\kappa_{ij} = \|C_{t_j} b_j\|^2_{Q_{tt}} - \|C_{t_i} b_i\|^2_{Q_{tt}}$. From the above, two conclusions can be made: (1) t lies in the hyperplane as defined by (59); (2) $C_{t_i} b_i = C_{t_j} b_j$. With $\underline{t}_{ij} = 2(C_{t_j} b_j - C_{t_i} b_i)^T Q_{tt}^{-1} \underline{t}$ being a continuous random variable with *nonzero* variance, its probability being equal to the constant value κ_{ij} is zero, i.e $\mathrm{P}(\underline{t} \in \mathcal{P}^{\mathrm{I}}_{ij}) = 0$. Therefore, the probability of the occurrence of the former conclusion is zero. Also, the latter conclusion contradicts our earlier assumption of $C_i b_i - C_j b_j \neq Av$ for all $v \in \mathbb{R}^n$. Therefore, $\mathcal{P}^{\mathrm{I}}_i \cap \mathcal{P}^{\mathrm{I}}_j = \emptyset$ for any $i \neq j$.

'only if' part: Let us assume that there exists some $v \in \mathbb{R}^n$ so that $C_i b_i - C_j b_j = Av$, and hence $C_{t_i} b_i = C_{t_j} b_j$, which implies that $S^{\mathrm{I}}_i = S^{\mathrm{I}}_j$ for all $t \in \mathbb{R}^r$. This reveals that $\mathcal{P}^{\mathrm{I}}_i = \mathcal{P}^{\mathrm{I}}_j$ which contradicts our earlier assumption of $\mathcal{P}^{\mathrm{I}}_i \cap \mathcal{P}^{\mathrm{I}}_j = \emptyset$. Therefore, $C_i b_i - C_j b_j \neq Av$ for all $v \in \mathbb{R}^n$, and any $i \neq j$. □

Proof of Lemma 3 'if' part: Let us assume that $\mathcal{P}^{\mathrm{II}}_{ij} = \mathcal{P}^{\mathrm{II}}_i \cap \mathcal{P}^{\mathrm{II}}_j \neq \emptyset$ for $i \neq j$. Then, for some $t \in \mathbb{R}^r$, we have

$$\|t - C_{t_i} b_i\|^2_{Q_{tt}} - \ln[\mathcal{P}[\mathcal{H}_i]]^2 = \|t - C_{t_j} b_j\|^2_{Q_{tt}} - \ln[\mathcal{P}[\mathcal{H}_j]]^2 \tag{60}$$

or alternatively

$$2(C_{t_j} b_j - C_{t_i} b_i)^T Q_{tt}^{-1} t = \kappa_{ij} \tag{61}$$

with $\kappa_{ij} = \|C_{t_j} b_j\|^2_{Q_{tt}} - \|C_{t_i} b_i\|^2_{Q_{tt}} - \ln[\mathcal{P}[\mathcal{H}_j]]^2 + \ln[\mathcal{P}[\mathcal{H}_i]]^2$. From the above, two conclusions can be made: (1) t lies in the hyperplane as defined by (61); (2) $C_{t_i} b_i = C_{t_j} b_j$ and $\mathcal{P}[\mathcal{H}_i] = \mathcal{P}[\mathcal{H}_j]$. With $\underline{t}_{ij} = 2(C_{t_j} b_j - C_{t_i} b_i)^T Q_{tt}^{-1} \underline{t}$ being a continuous random variable with *nonzero* variance, its probability being equal to the constant value κ_{ij} is zero, i.e $\mathsf{P}(\underline{t} \in \mathcal{P}^{\mathrm{II}}_{ij}) = 0$. Therefore, the former conclusion has zero probability of occurring. Also, the latter conclusion contradicts our earlier assumptions (1) and (2). Therefore, $\mathcal{P}^{\mathrm{II}}_i \cap \mathcal{P}^{\mathrm{II}}_j = \emptyset$ for any $i \neq j$.

'only if' part: Let us assume that $\mathsf{P}[\mathcal{H}_i] = \mathsf{P}[\mathcal{H}_j]$ and that there exists some $v \in \mathbb{R}^n$ so that $C_i b_i - C_j b_j = Av$, and hence $C_{t_i} b_i = C_{t_j} b_j$. Therefore, we have $S^{\mathrm{II}}_i = S^{\mathrm{II}}_j$ for all $t \in \mathbb{R}^r$, which reveals that $\mathcal{P}^{\mathrm{II}}_i = \mathcal{P}^{\mathrm{II}}_j$. This however contradicts our earlier assumption of $\mathcal{P}^{\mathrm{II}}_i \cap \mathcal{P}^{\mathrm{II}}_j = \emptyset$. Therefore, at least one of (1) and (2) should hold true. □

Author Contributions S.Z. and P.J.G.T. contributed to the design, implementation of the research, analysis of the results and the writing of the manuscript.

Funding Open Access funding enabled and organized by CAUL and its Member Institutions

Data Availability No data are used for this study.

References

Amiri Simkooei A (2001) Comparison of reliability and geometrical strength criteria in geodetic networks. J Geodesy 75(4):227–233

Baarda W (1968) A testing procedure for use in geodetic networks. Netherlands Geodetic Commission, Publ on geodesy, New Series 2(5)

Costa A, Magalhães M, Epprecht EK (2010) Th e Non-Central Chi-Square Chart with Double Sampling. Braz J Oper & Prod Manag 2:21–38

DGCC (1982) The Delft Approach for the Design and Computation of Geodetic Networks. In: "Forty Years of Thought" Anniversary edition on the occasion of the 65th birthday of Prof W Baarda, By staff of the Delft Geodetic Computing Centre (DGCC), 2, pp 202–274

Gillissen I, Elema IA (1996) Test results of DIA: a real-time adaptive integrity monitoring procedure, used in an integrated naviation system. The International Hydrographic Review

Haynam G, Govindarajulu Z, Leone F, Siefert P (1982) Tables of the cumulative non-central chi-square distribution-part l. Stat J Theor Appl Stat 13(3):413–443

Hewitson S, Wang J (2006) GNSS receiver autonomous integrity monitoring (RAIM) performance analysis. GPS Solutions 10(3):155–170

Jonkman N, De Jong K (2000) Integrity monitoring of igex-98 data, part II: cycle slip and outlier detection. GPS Solutions 3(4):24–34

Khodabandeh A, Teunissen PJG (2016) Single-epoch GNSS array integrity: An analytical study. In: Sneeuw N, Novák P, Crespi M, Sansò F (eds) VIII Hotine-Marussi Symposium on Mathematical Geodesy: Proceedings of the Symposium in Rome, 17-21 June, 2013, Springer International Publishing, pp 263–272

Kroese DP, Taimre T, Botev ZI (2011) Handbook of Monte Carlo Methods. Wiley Series in Probability and Statistics

Kuusniemi H, Lachapelle G, Takala JH (2004) Position and velocity reliability testing in degraded GPS signal environments. GPS Solutions 8(4):226–237

Lehmann R, Lösler M (2017) Congruence analysis of geodetic networks-hypothesis tests versus model selection by information criteria. J Appl Geod 11(4):271–283

Nowel K (2020) Specification of deformation congruence models using combinatorial iterative DIA testing procedure. J Geodesy 94(12):1–23

Robert C, Casella G (2004) Monte Carlo Statistical Methods. Springer, Berlin

Rofatto VF, Matsuoka MT, Klein I, Bonimani M, Rodrigues BP, de Campos CC, Veronez MR, da Silveira Jr LG (2022) An artificial neural network-based critical values for multiple hypothesis testing: data-snooping case. Surv Rev 54(386):440–455

Teunissen PJG (1990) An integrity and quality control procedure for use in multi-sensor integration. In: Proc. of ION GPS-1990, ION, pp 513–522

Teunissen PJG (2017) Batch and Recursive Model Validation. In: Teunissen PJG, Montenbruck O (eds) Springer Handbook of Global Navigation Satellite Systems, chap 24, pp 727–757

Teunissen PJG (2018) Distributional theory for the DIA method. J Geodesy 92(1):59–80. https://doi.org/10.1007/00190-017-1045-7

Teunissen PJG (2024a) On the optimality of DIA-estimators: theory and applications. J Geodesy 98(43):1–26. https://doi.org/10.1007/00190-024-01859-w

Teunissen PJG (2024b) Testing Theory: an introduction. 3rd Edition, TUDelft OPEN Textbooks https://doi.org/10.59490/tb.96

Verhoef H, De Heus HM (1995) On the estimation of polynomial breakpoints in the subsidence of the Groningen gasfield. Surv Rev 33(255):17–30

Yang L, Li Y, Wu Y, Rizos C (2014) An enhanced MEMS-INS/GNSS integrated system with fault detection and exclusion capability for land vehicle navigation in urban areas. GPS Solutions 18(4):593–603

Yang L, Shen Y, Li B, Rizos C (2021) Simplified algebraic estimation for the quality control of DIA estimator. J Geodesy 95:1–15

Yavaşoğlu HH, Kalkan Y, Tiryakioğlu I, Yigit CO, Özbey V, Alkan MN, Bilgi S, Alkan RM (2018) Monitoring the deformation and strain analysis on the Ataturk Dam, Turkey. Geomat Nat Haz Risk 9(1):94–107

Zaminpardaz S, Teunissen PJG (2019) DIA-datasnooping and identifiability. J Geodesy 93(1):85–101. https://doi.org/10.1007/s00190-018-1141-3

Zaminpardaz S, Teunissen PJG (2022) On the computation of confidence regions and error ellipses: a critical appraisal. J Geodesy 96(2):10

Zaminpardaz S, Teunissen PJG, Tiberius CCJM (2020) A risk evaluation method for deformation monitoring systems. J Geodesy 94(3):28

Zaminpardaz S, Teunissen PJG (2020) GNSS Detection and Estimation Integrity, Springer International Publishing, Cham, pp 1–9. https://doi.org/10.1007/978-3-319-02370-0_170-1